

# Materials Advances

Accepted Manuscript

This article can be cited before page numbers have been issued, to do this please use: K. Mego, E. Accardo, P. Ruiz-Campos, H. Garcia Baldovi and P. Atienzar, *Mater. Adv.*, 2026, DOI: 10.1039/D5MA01122A.



This is an Accepted Manuscript, which has been through the Royal Society of Chemistry peer review process and has been accepted for publication.

Accepted Manuscripts are published online shortly after acceptance, before technical editing, formatting and proof reading. Using this free service, authors can make their results available to the community, in citable form, before we publish the edited article. We will replace this Accepted Manuscript with the edited and formatted Advance Article as soon as it is available.

You can find more information about Accepted Manuscripts in the [Information for Authors](#).

Please note that technical editing may introduce minor changes to the text and/or graphics, which may alter content. The journal's standard [Terms & Conditions](#) and the [Ethical guidelines](#) still apply. In no event shall the Royal Society of Chemistry be held responsible for any errors or omissions in this Accepted Manuscript or any consequences arising from the use of any information it contains.

# CsPbBr<sub>3</sub> nanocrystals supported on partially oxidized Ti<sub>2</sub>N MXenes for photothermal CO<sub>2</sub> conversion

View Article Online  
DOI: 10.1039/DMA01122A

Kevin Mego<sup>1</sup>, Emanuela Accardo<sup>2</sup>, Pedro Ruiz-Campos<sup>3</sup>, Herme G. Baldovi<sup>2\*</sup> and Pedro Atienzar<sup>1\*</sup>

<sup>1</sup> Instituto de Tecnología Química, Consejo Superior de Investigaciones Científicas, Universitat Politècnica de València, Avenida de los Naranjos s/n, 46022 Valencia, Spain

<sup>2</sup> Departamento de Química, Universitat Politècnica de València, Camino de Vera s/n, 46022 Valencia, Spain

<sup>3</sup> Universidad Científica del Sur, Panamericana Sur Km 19, 150142 Lima, Perú

**Corresponding author:** Pedro Atienzar ([pedatcor@itq.upv.es](mailto:pedatcor@itq.upv.es)) | Hermenegildo García Baldoví ([hergarba@itq.upv.es](mailto:hergarba@itq.upv.es))

**Keywords:** photocatalysis, perovskites, partially oxidized MXenes, charge transfer

## Abstract:

The development of new photo-thermal catalysts for the transformation of CO<sub>2</sub> into fuels is of great interest, offering a clean and sustainable approach to reducing the carbon footprint. Herein, we present a novel hybrid material composed of nanocrystalline metal halide perovskite (CsPbBr<sub>3</sub>) supported on two-dimensional titanium nitride (Ti<sub>2</sub>N) MXene. Additionally, we demonstrate the importance of forming an external TiO<sub>2</sub> layer through partial oxidation of the MXene (POM-Ti<sub>2</sub>N), which introduces catalytic centers and enhances photogenerated charge separation. Remarkable activity in the formation of CH<sub>4</sub> and CO was observed, with yields of 321 μmol·g<sup>-1</sup> and 480 μmol·g<sup>-1</sup>, respectively. The selectivity of the reaction was found to be temperature dependent. The mechanism was thoroughly investigated using XPS and photoluminescence studies. XPS analysis revealed a significant chemical interaction between the CsPbBr<sub>3</sub> nanocrystals and the POM-Ti<sub>2</sub>N MXene after the formation of the composite. Photoluminescence measurements revealed a considerably shorter emission lifetime for the hybrid catalyst ( $\tau_{ave} = 1.73$  ns) compared to that of the CsPbBr<sub>3</sub> nanoparticles ( $\tau_{ave} = 25.32$  ns), indicating strong interaction with the MXene. Furthermore, this research highlights the potential of combining metal halide perovskites with MXenes and the importance of controlling their interface for photo-thermal reactions.

## 1. Introduction

View Article Online  
DOI: 10.1039/D5MA01122A

Researchers are making significant efforts to address climate change by developing CO<sub>2</sub> utilization technologies that convert this molecule into chemicals. Solar-driven photothermal catalysis is a compelling and sustainable approach that harnesses light and heat energy to synergetically convert CO<sub>2</sub> into fuels and valuable chemicals.<sup>1,2</sup> There are many photothermal catalytic pathways that offer sustainable routes for CO<sub>2</sub> valorization,<sup>3,4</sup> such as the Sabatier reaction, which has been one of the most studied reactions for over a century since its discovery. This reaction consists of the hydrogenation of CO<sub>2</sub> to CH<sub>4</sub>, which is thermodynamically favorable but is hindered by slow reaction kinetics, therefore, the use of high temperatures is necessary to activate the CO<sub>2</sub> molecule. The photothermal catalytic mechanism includes multiple proton-coupled electron transfer to CO<sub>2</sub> to form CH<sub>4</sub>, which requires control of intermediate species on catalytic surfaces, often resulting in reduced selectivity and lower overall activity.<sup>5</sup>

In the classical thermal methanation process, the most studied metallic active centers are Ni, Ru, and Rh, which require high temperatures (300 to 400 °C) and pressures (5-20 bar) to achieve high efficiencies. However, the photothermal pathway can promote the Sabatier reaction under milder conditions, employing the same active sites supported on a semiconductor, with metal oxides being the most commonly used due to their robustness under reaction conditions. Recent studies showed that nickel (Ni) has emerged as the optimal compromise, delivering Ru-like activity when properly nanostructured on TiO<sub>2</sub> or CeO<sub>2</sub> supports.<sup>6-8</sup> Other researchers used single atoms and nanoparticles of ruthenium supported on CeAlO<sub>x</sub>, achieving formidable catalytic performances.<sup>9</sup> Although a huge number of materials have been already explored to boost the photocatalytic side of the photothermal reaction (e.g. metal oxide, MOFs, COFs, metal complex, C<sub>3</sub>N<sub>4</sub>...)<sup>10-13</sup> there is still a need to boost this reaction at lower temperatures (< 250 °C).

Metal halide perovskite nanocrystals (NCs) semiconductors have been extensively studied because they offer a wide range of applications due to their excellent optoelectronic properties, such as broad absorption in the UV-Vis spectrum, tuneable light absorption range, long charge diffusion length, and high molar extinction coefficients.<sup>14</sup> All these properties make them potential candidates for multiple photocatalytic applications. However, to improve the photocatalytic activity of pristine CsPbBr<sub>3</sub>, it has been combined with other materials, on the one hand, to improve charge separation properties through charge migration and, on the other hand, to add better active catalytic sites.<sup>15,16</sup> In this regard, MXenes materials as a new type of two-dimensional (2D) structure, have recently attracted great attention due to their interesting

properties such as rich surface chemistry, modifiable electronic structure and thermal stability. MXenes are transition metal carbides or nitrides with the general formula  $M_{n+1}X_nT_x$  ( $n=1, 2$  or  $3$ ), where  $M$  corresponds to a transition metal,  $X$  can be C or N, and  $T_x$  indicates the surface functional groups (usually -F, -O or -OH). These functional groups play an important role in the adsorption/desorption of molecules and electron transfer properties. Currently, in photothermal reduction of  $CO_2$ , there are a few examples in the literature studying the catalytic properties of MXene carbides containing perovskite NCs. For instance, aerogels of  $CsPbBr_3/Ti_3C_2Tx$  MXene showed that  $Ti_3C_2Tx$  MXene's conductive network promotes charge separation from photoexcited  $CsPbBr_3$ , while its surface terminations (-O, -F, -OH) improve  $CO_2$  adsorption, outperforming individual components.<sup>17</sup>

In addition, partially oxidized 2D transition metal carbides MXenes, also offer the possibility to decorate the titanium nitride MXene with  $TiO_2$  moieties. According to the work of Pazniak et al.<sup>18</sup>, the enhanced charge carrier exchange at the  $TiO_2$ /MXene interface enhances the sensing properties due to the formation of a depletion region between the metal and the semiconductor interface.<sup>19</sup>

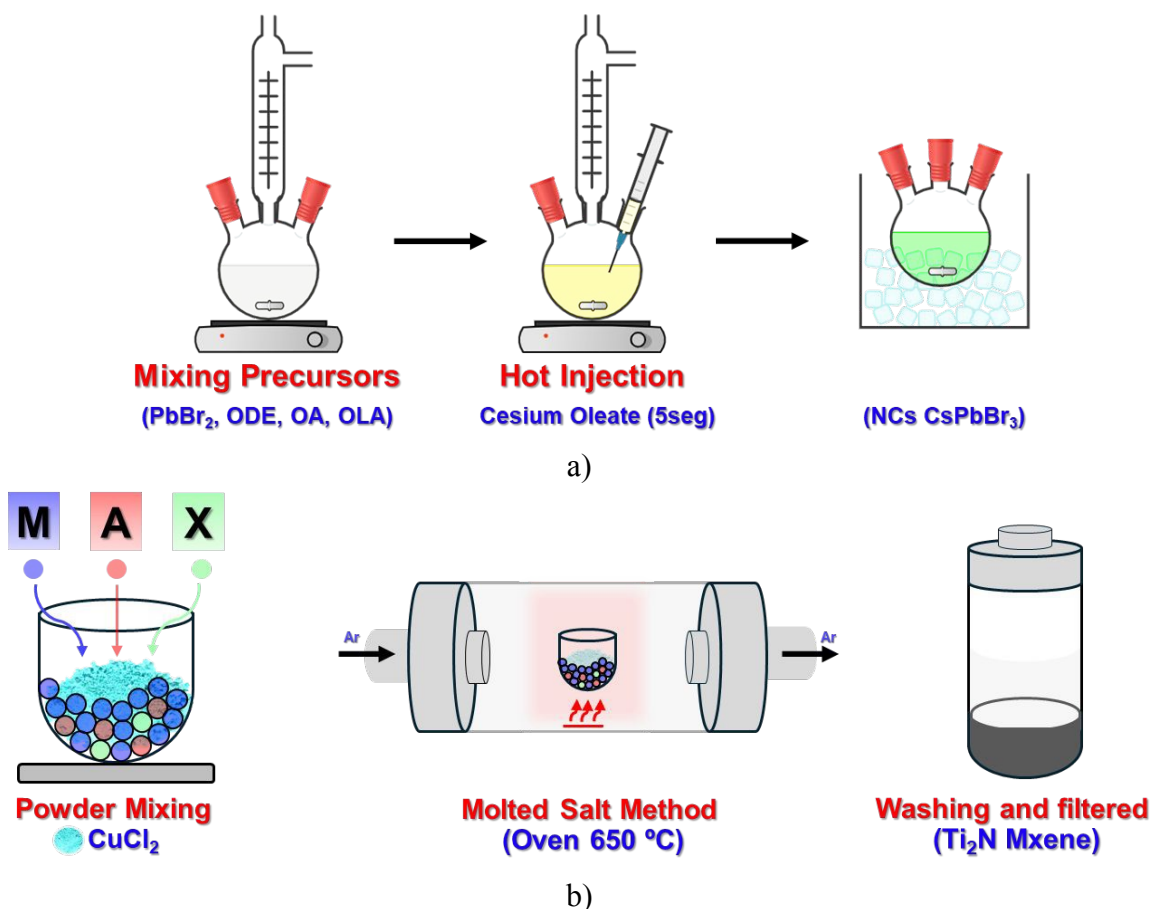
The novelty of this work rely in the use for the first time of titanium nitride ( $Ti_2N$ ) MXene in the Sabatier reaction. Therefore, within this context, we have been the first investigating the formation of a novel hybrid material composed of nanocrystalline  $CsPbBr_3$  supported on two-dimensional titanium nitride ( $Ti_2N$ ) MXene for photo-thermal  $CO_2$  conversion. To date, there is no report describing this specific combination. Although bare metal nitride MXenes can exhibit certain limitations in this reaction, we addressed this by forming external  $TiO_2$  moieties through partial oxidation of the  $Ti_2N$  MXene and combining it with the perovskite nanocrystals. We evaluated the catalytic activity under different conditions and assessed its reusability, concluding that this hybrid is capable of performing  $CO_2$  revalorization. XPS analysis and photophysical studies were carried out. Finally, we propose a working mechanism based on the formation of a heterojunction architecture, featuring an interlayer that inhibits direct charge recombination.

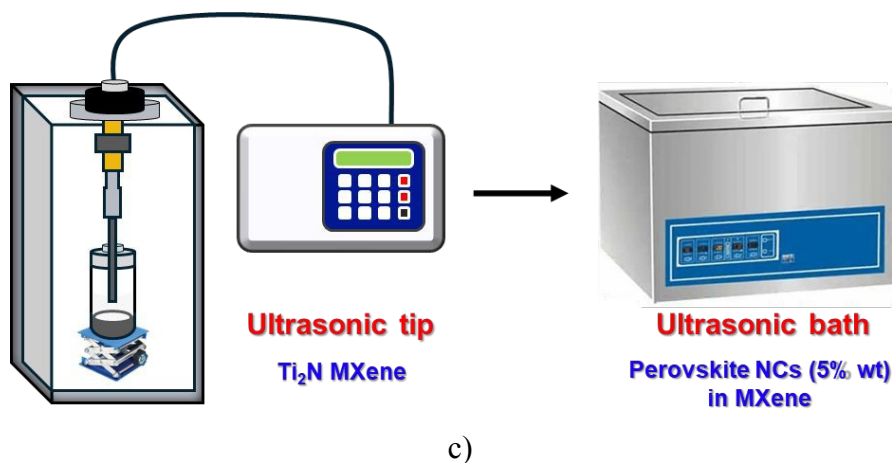
## 2. Results and discussion

$CsPbBr_3$  perovskite NCs and the  $Ti_2N$  MXenes were prepared separately according to the synthetic procedure described in detail in the Materials and Methods (see Supporting Information) and illustrated in Scheme 1. The synthesis of  $CsPbBr_3$  NCs was carried out by the hot injection method<sup>20</sup>. Scheme 1a) shows the conventional preparation of the NCs through

three sequential steps: i) mixing the precursors in a three-neck flask at elevated temperature, ii) rapid injection of the cesium precursor, and iii) immediate quenching in an ice-cold water bath. Regarding the preparation of partially oxidized multilayer  $\text{Ti}_2\text{N}$  MXene (POM- $\text{Ti}_2\text{N}$ ) involves two main stages: i) first the MAX phase was treated with  $\text{CuCl}_2$  using the molten salt method at high temperature ( $650\text{ }^\circ\text{C}$ ), followed by copper removal using persulfate solution, and ii) afterwards the solid was filtered and thoroughly washed with deionized water. It is during the purification with persulfates salts at  $70\text{ }^\circ\text{C}$ , when a thin layer of small nanoparticles of  $\text{TiO}_2$  were grown on top of the surface resulting in the partial oxidation of the  $\text{T}_2\text{N}$  MXene. (see Scheme 1b). Actually,  $\text{TiO}_2$  presence is residual if the purification is carried out during same time and at room temperatures.

Finally, the perovskite NCs were supported onto POM- $\text{Ti}_2\text{N}$  by after dispersing the POM- $\text{Ti}_2\text{N}$  with ultrasonication in hexane and added dropwise a concentrated suspension of NCs. After a time, the solid was recovered by filtration. More details are described in the Materials and Methods (Scheme 1c).





**Scheme 1.** Synthetic procedure for the preparation of the catalyst. a) Preparation of the CsPbBr<sub>3</sub> NCs, b) Formation of the Ti<sub>2</sub>N MXene from the MAX phase and c) impregnation process for the deposition of the CsPbBr<sub>3</sub> NCs on the exfoliated Ti<sub>2</sub>N MXene.

The synthesis of M-Ti<sub>2</sub>N was carried out according to publication by Xinbo Liu et al., following the molten salt method, in which molar ratios between 1:3 and 1:4 with respect to Ti<sub>2</sub>NaI:CuCl<sub>2</sub> are used. In our case, ratios of 1:4 were chosen to synthesise the multi-layered T<sub>2</sub>N MXene.<sup>21</sup> In fact, analysis carried out with X-ray diffraction spectroscopy shown in Figure S4, confirms that the titanium nitride MXene synthesized by the molten salt method leads to a nitride with the crystal structure of  $\alpha$ -TiN with characteristic peaks at 37.9°, 43.3° and 62.7° according, respectively, to the planes (004), (103), and (110).<sup>22,23</sup>

A slight modification of the purification procedure during the bath with persulphate salts, such as raising the temperature of the process or increasing the concentration of this salt, leads to a modification of the chemistry of the surface of the MXene layers by superficially oxidising the M-Ti<sub>2</sub>N layers as can also be seen in Figure S4 with the appearance of new TiO<sub>2</sub>-related signals, at  $2\theta = 25.3^\circ$ ,  $47.9^\circ$ ,  $54.4^\circ$  and  $2\theta = 27.4^\circ$ ,  $43.3^\circ$  assigned to (101), (202), (211) anatase and (110), (111) rutile crystalline planes.

Furthermore, XRD analyses were performed for all the materials. The XRD results were trustworthy with the ICSD data file, #204325<sup>24</sup> which confirms the cubical crystalline structure of the CsPbBr<sub>3</sub> NCs, evidenced by the presence of the peaks at the angles 15° and 30°, which represent the (001) and (002) crystalline planes of the cubic perovskite crystals (Figure 1b). Once the NCs@POM-Ti<sub>2</sub>N composite has been formed, it is not possible to visualise the signals due to the NCs due to their low concentration in the sample (<5% by weight) and the small amount of material used during the analysis (Figure 1a).

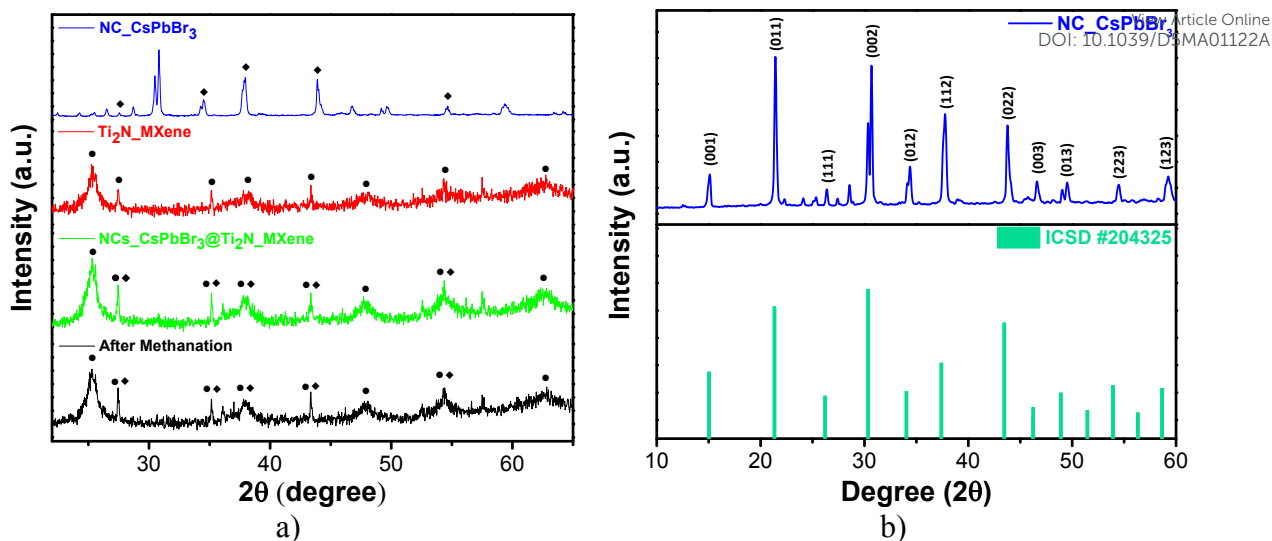


**Figure 1.** a) Comparative XRD pattern of CsPbBr<sub>3</sub> NCs (blue), POM-Ti<sub>2</sub>N MXene (red), NCs@POM-Ti<sub>2</sub>N before (green) and after the catalytic reaction (black), b) CsPbBr<sub>3</sub> NCs compared with reference data from the ICSD #204325 data file.

Moreover, high-resolution transmission electron microscopy (HR-TEM) was used to study the CsPbBr<sub>3</sub> NCs and the Ti<sub>2</sub>N MXene independently. Figure 2a shows that the perovskites NCs particles have a similar size and crystallinity. The particle size distribution of NCs was estimated using HR-TEM, yielding an average size of 5 nm (Figure 2b).

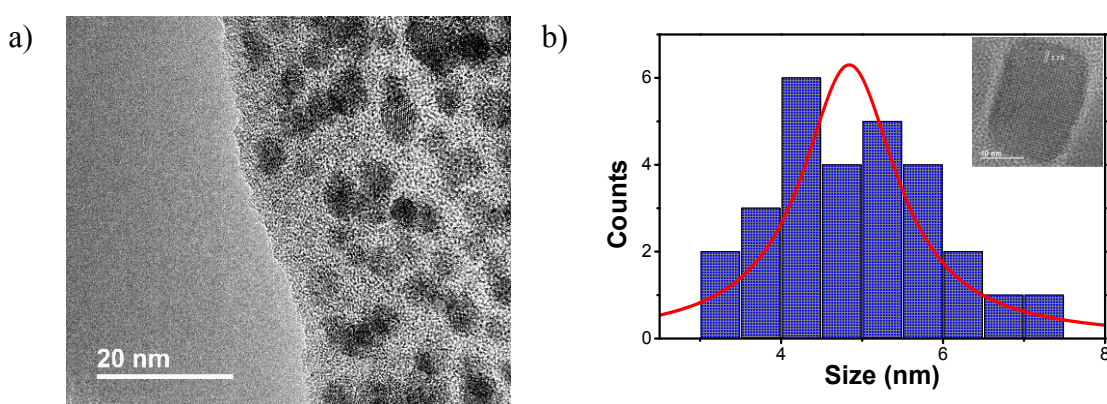
High resolution field emission scanning electron microscopy (HR-FESEM) is a useful tool to distinguish between the formation of multi-layered Ti<sub>2</sub>N MXene (M-Ti<sub>2</sub>N) and POM-Ti<sub>2</sub>N. A soft purification treatment with 0.1M of sodium persulfate at room temperature leads easily to purification of M-Ti<sub>2</sub>N with a minor structural defect, as shown in Figure 2c; whereas the same concentration of persulfate, but treating the MXene at 70 °C, produced a slight oxidation of the MXene surface, forming the POM-Ti<sub>2</sub>N (see Figure 2d). Also, HR-FESEM images in Figure S5 reveal the formation of rugosity on the surface and edges of the Ti<sub>2</sub>N MXene layers with the appearance of little crystals of TiO<sub>2</sub> homogenously dispersed. Additionally, interplanar distances measured with HR-TEM on layers of the POM-T<sub>2</sub>N sample confirm the simultaneous presence of Ti<sub>2</sub>N and TiO<sub>2</sub> crystals. (Figure 2e) After the formation of the composite NCs@POM-Ti<sub>2</sub>N no evident changes are seen by HR-FESEM in the partially oxidized MXene particle; (Figure 2f) however, the dispersion of NCs particles on the POM-Ti<sub>2</sub>N MXene is confirmed with DF STEM images in Figure S6. This image showed that elements that form the perovskite particles are well dispersed and distributed homogenously over the support. A clearer image that shows the physical presence of perovskites NCs on the POM-Ti<sub>2</sub>N support is shown in Figure S7, from which we can estimate a loading of 5% per weight of NCs on the POM-Ti<sub>2</sub>N MXene.

To elucidate the fine structure of the hybrid, HR-TEM images of NCs@POM-Ti<sub>2</sub>N are presented in Figure 2g-h. As shown in Figure 2g, TiO<sub>2</sub> nanoparticles are uniformly anchored onto the Ti<sub>2</sub>N MXene sheets, forming a surface-decorated<sup>25</sup> hybrid. This observation confirms that the partial surface transformation of Ti<sub>2</sub>N into TiO<sub>2</sub> occurs during processing, yielding a coherent TiO<sub>2</sub>/Ti<sub>2</sub>N heterostructure.<sup>26</sup>

The distinct lattice fringes observed for both phases further verify the successful formation of the composite (Figure 2h). Spacings of 3.50 Å and 2.70 Å, as well as 2.10 Å, correspond to the (101) planes of anatase TiO<sub>2</sub><sup>26</sup> and the (01 $\bar{1}$ 0) planes of Ti<sub>2</sub>N,<sup>27,28</sup> respectively. In addition, the lattice fringes of 3.00 Å are assigned to the (200) planes of CsPbBr<sub>3</sub> nanocrystals,<sup>29</sup> indicating their favourable deposition across the entire TiO<sub>2</sub>/Ti<sub>2</sub>N MXene surface.

Interestingly, the Ti<sub>2</sub>N nanosheets appear partially intercalated among the surface-grown TiO<sub>2</sub> nanoparticles, generating a textured template onto which CsPbBr<sub>3</sub> NCs are subsequently anchored. This morphological arrangement is entirely consistent with the structural model illustrated in Figure 8a for NCs@POM-Ti<sub>2</sub>N. Such an architecture provides an enlarged interfacial contact area, thereby facilitating efficient charge-carrier migration throughout the heterostructure.

The thermal stability of CsPbBr<sub>3</sub> and POM-Ti<sub>2</sub>N MXene was investigated using thermogravimetric analysis (TGA) (Figure S8). The results indicate that POM-Ti<sub>2</sub>N MXene exhibits high thermal stability, showing only a small percentage of weight loss over the entire temperature range studied. In addition, CsPbBr<sub>3</sub> (NCs) shows a sharp weight loss around 600 °C, indicating thermal stability up to this temperature. All of the above indicates the stability of the materials under the catalytic conditions studied.



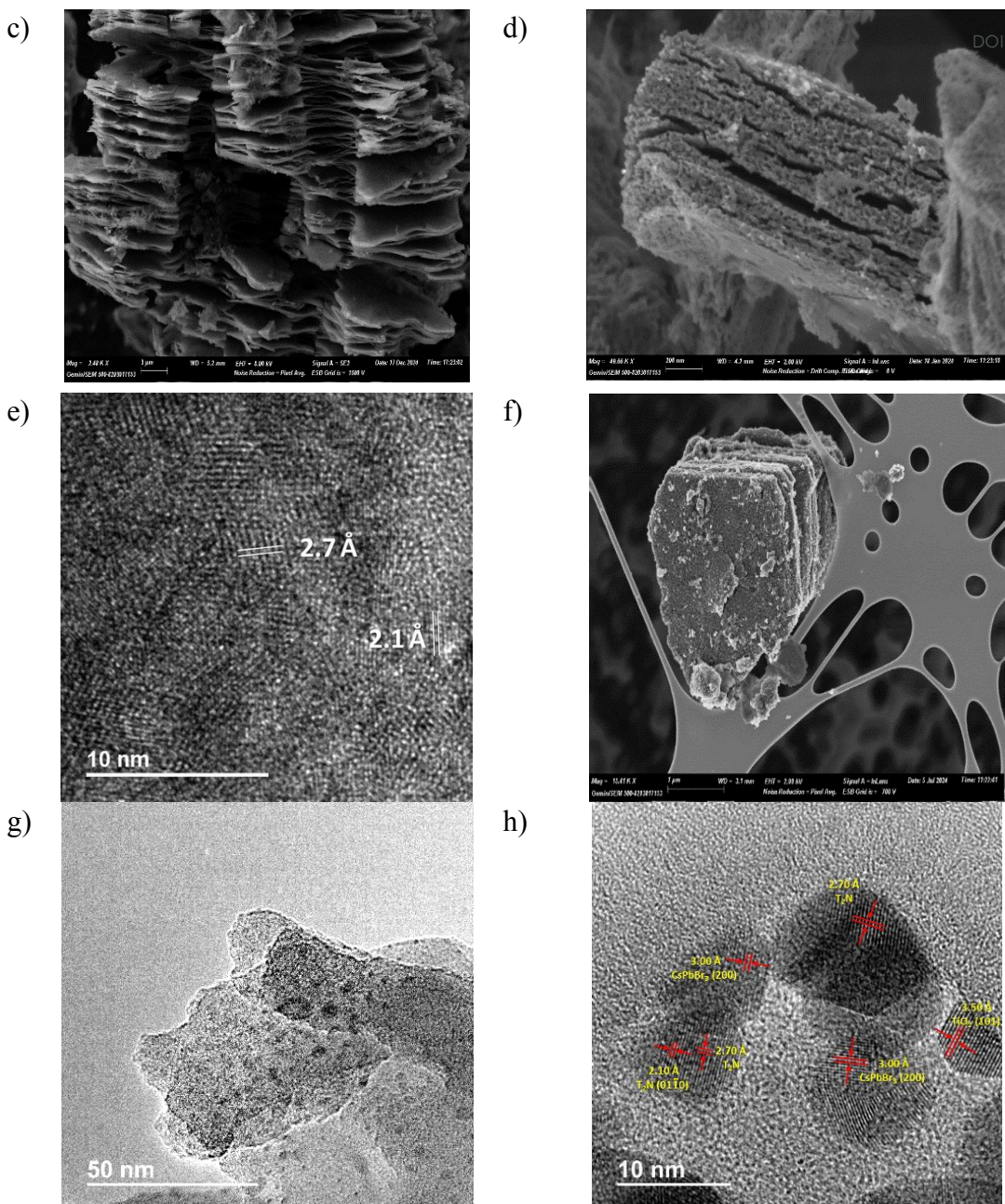


**Figure 2.** a) HR-TEM image showing the lead halide perovskites ( $\text{CsPbBr}_3$ ) nanocrystals. (b) Histogram for the size distribution of the  $\text{CsPbBr}_3$  NCs, the inset shows enlarged individual NCs, c) HR-FESEM image of  $\text{Ti}_2\text{N}$  MXene, d) HR-FESEM picture of the POM- $\text{Ti}_2\text{N}$ , e) HR-TEM of a layer of POM- $\text{Ti}_2\text{N}$  with different interplanar distances f) HR-FESEM images of the composite NCs@POM- $\text{Ti}_2\text{N}$ . g) TEM image showing  $\text{CsPbBr}_3$  NCs distributed across  $\text{Ti}_2\text{O}/\text{Ti}_2\text{N}$  MXene. h) Corresponding high-resolution (HR-TEM) image of NC@POM- $\text{Ti}_2\text{N}$  displaying the lattice fringes assigned to anatase  $\text{TiO}_2$  ( $3.50 \text{ \AA}$ , (101)),  $\text{Ti}_2\text{N}$  MXene ( $2.70 \text{ \AA}$  and  $2.10 \text{ \AA}$ , (0110)), and  $\text{CsPbBr}_3$  nanocrystals ( $3.00 \text{ \AA}$ , (200)), confirming the formation of the  $\text{Ti}_2\text{O}/\text{Ti}_2\text{N}$  heterostructure decorated with  $\text{CsPbBr}_3$  NCs.



The surface change induced by the partial oxidation of M-Ti<sub>2</sub>N produces profound changes in the optical absorption of the material. As shown in Figure S9, when titanium nitride is present, the absorbance spans the UV region to the entire visible range. However, when oxidation occurs, its absorbance becomes significantly more prominent in the UV region up to 380 nm due to the appearance of TiO<sub>2</sub> domains on the M-Ti<sub>2</sub>N structure. For the sake of comparison, diffuse reflectance UV-Vis spectroscopy of perovskite NCs, POM-Ti<sub>2</sub>N MXene, and composite NCs@POM-Ti<sub>2</sub>N are also plotted in Figure 3. Herein, we can see the POM-Ti<sub>2</sub>N MXene UV-Vis spectra exhibiting a strong band absorption with an edge at 380 nm, characteristic of TiO<sub>2</sub> absorption. In the case of CsPbBr<sub>3</sub> NCs, they display characteristic UV-Vis absorption within the wavelength range of  $\lambda < 540$  nm. The UV-Vis spectrum also verifies the formation of the composite NCs and POM-Ti<sub>2</sub>N MXene as the supported material combines both absorptions, expanding the photophysical response of the initial POM-Ti<sub>2</sub>N in the visible region.

The optical band gaps ( $E_g$ ) of the synthesized materials were determined using UV-Vis diffuse reflectance spectroscopy (DRS), analyzed through Tauc plot extrapolations (Figure S10, Supporting Information).<sup>30</sup> The extracted band gap values were found to be 2.28 eV<sup>31</sup> for CsPbBr<sub>3</sub> NCs and 3.26 eV for the POM-Ti<sub>2</sub>N, respectively.

To further elucidate the superior optoelectronic behavior of the perovskite material, the valence band edge positions ( $E_v^{\text{NHE}}$ ) relative to the normal hydrogen electrode (NHE) were investigated using X-ray photoelectron spectroscopy (XPS).<sup>32-34</sup> The  $E_v^{\text{NHE}}$  values were calculated based on Equation (1):

$$E_v^{\text{NHE}} = E_v^f + \varphi_{sp} + E_0^{\text{NHE}} \quad (1)$$

where  $E_v^f$  is the Fermi level of the material determined from XPS measurements,  $\varphi_{sp}$  is the spectrometer work function (4.244 eV), and  $E_0^{\text{NHE}}$  is the energy level of the standard hydrogen electrode relative to the vacuum level (-4.44 eV).

Based on the calculated valence band (VB) positions and the corresponding optical band gaps, the conduction band minimum (CB) energies were inferred for each material. The estimated VB potentials referenced to the NHE were 1.14 eV for CsPbBr<sub>3</sub> NCs and 2.30 eV for POM-Ti<sub>2</sub>N, as shown in Figure S11(a, b). Moreover, the CB values of CsPbBr<sub>3</sub> NCs and POM-Ti<sub>2</sub>N are -1.14 and -0.96 eV, respectively. Regarding the POM-Ti<sub>2</sub>N MXene material, we expect two distinct regions: an outer region corresponding to the partially oxidized Ti<sub>2</sub>N MXene with TiO<sub>x</sub> groups exhibiting electron-withdrawing behavior, and an inner region mainly of Ti<sub>2</sub>N MXene with a metallic character, which facilitates efficient electron extraction. Consequently, energy

band diagrams were constructed, providing comprehensive insight into the electronic structure of the materials investigated. (Figure 3b)

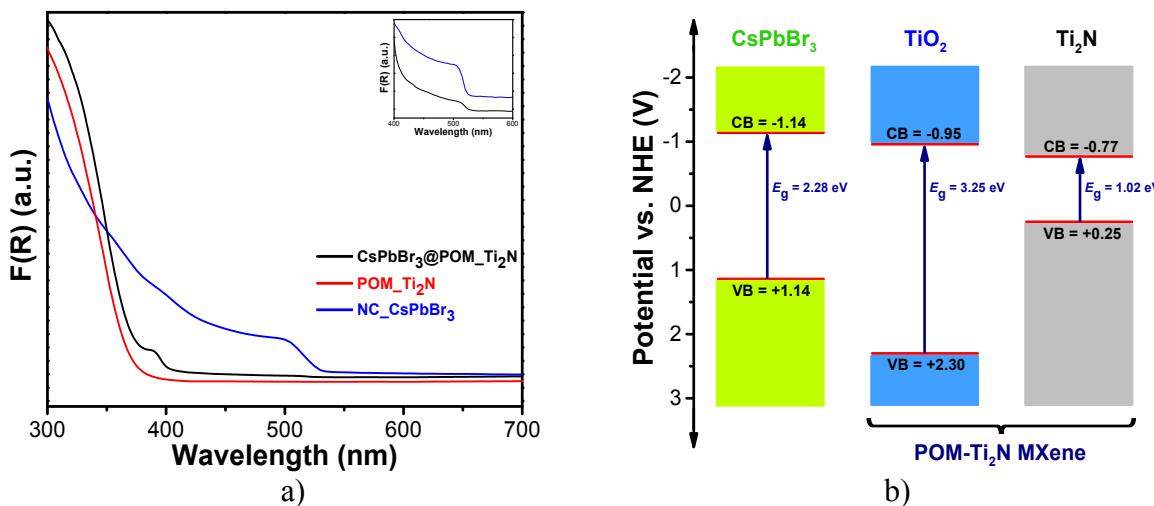


**Figure 3.** a) Diffuse reflectance UV-Vis optical spectra of CsPbBr<sub>3</sub> NCs, Ti<sub>2</sub>N MXene and the supported material. The Inset shows a magnification in the characteristic range of the CsPbBr<sub>3</sub> NCs absorption. b) Schematic energy band level diagram of each component of CsPbBr<sub>3</sub>@POM-Ti<sub>2</sub>N composite. The respective CB and VB values, as well as the optical band gaps (all in eV), are extracted from the XPS and UV-Vis measurements respectively.

With the aim to understand the mechanism of the catalytic process that occurs during the photo-thermal reaction, steady-state and lifetime emission were studied. The PL spectrum of the CsPbBr<sub>3</sub> NCs exhibits a strong emission peak at 530 nm; however, for the sample CsPbBr<sub>3</sub>@POM-Ti<sub>2</sub>N MXene, we observed a decrease in PL intensity along with a blue shift in the peak maximum to 513 nm. This shift to the blue can be attributed to the Burstein-Moss effect<sup>35</sup>. This effect is related to the change in carrier concentration caused by the electronic coupling between the perovskite nanocrystals and the MXene material. In addition, the decrease in emission intensity can be ascribed to the transfer of photogenerated carriers between the CsPbBr<sub>3</sub> NCs and the POM-Ti<sub>2</sub>N MXene.<sup>36</sup>

The time-resolved fluorescence spectroscopy (Figure 4) was used to investigate the lifetime emission of pure CsPbBr<sub>3</sub> NCS and the supported CsPbBr<sub>3</sub>@POM-Ti<sub>2</sub>N MXene catalyst. The best fitting corresponds to a biexponential decay model, where the short lifetime is attributed to nonradiative recombination of electron-hole pairs and surface trap states and the long lifetime to the radiative recombination.<sup>37,38</sup>

The emission lifetime of CsPbBr<sub>3</sub>@POM Ti<sub>2</sub>N MXene ( $\tau_{ave} = 1.73$  ns) was relatively shorter than that of the corresponding CsPbBr<sub>3</sub> nanoparticles ( $\tau_{ave} = 25.32$  ns). This difference in the emission lifetime between both materials indicates the emergence of a nonradiative pathway

from the significant electronic interaction between  $\text{CsPbBr}_3$  nanoparticles and partially oxidized MXene.<sup>18</sup> This provides an alternative interfacial pathway for the excited electrons of  $\text{CsPbBr}_3$  to transfer to the oxidized MXene and relax non-radiatively, allowing them to participate in the catalytic reaction.<sup>35,39</sup>

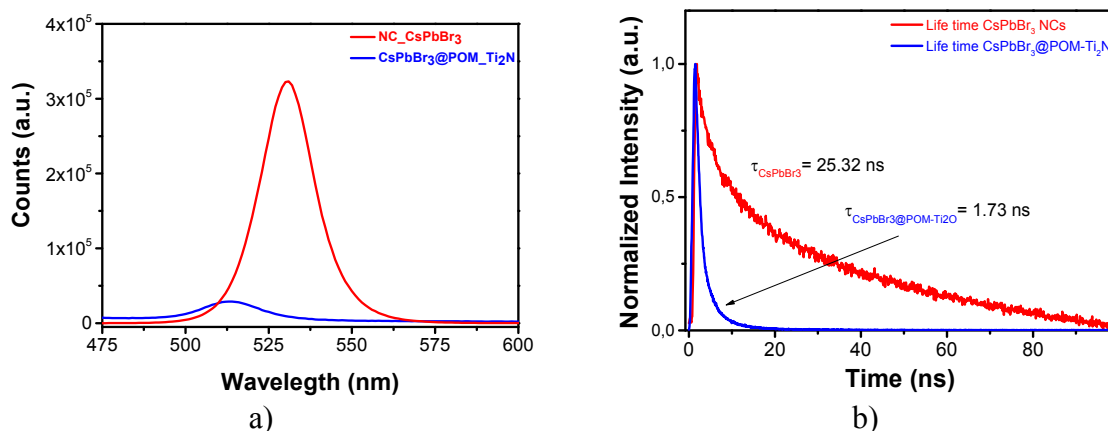
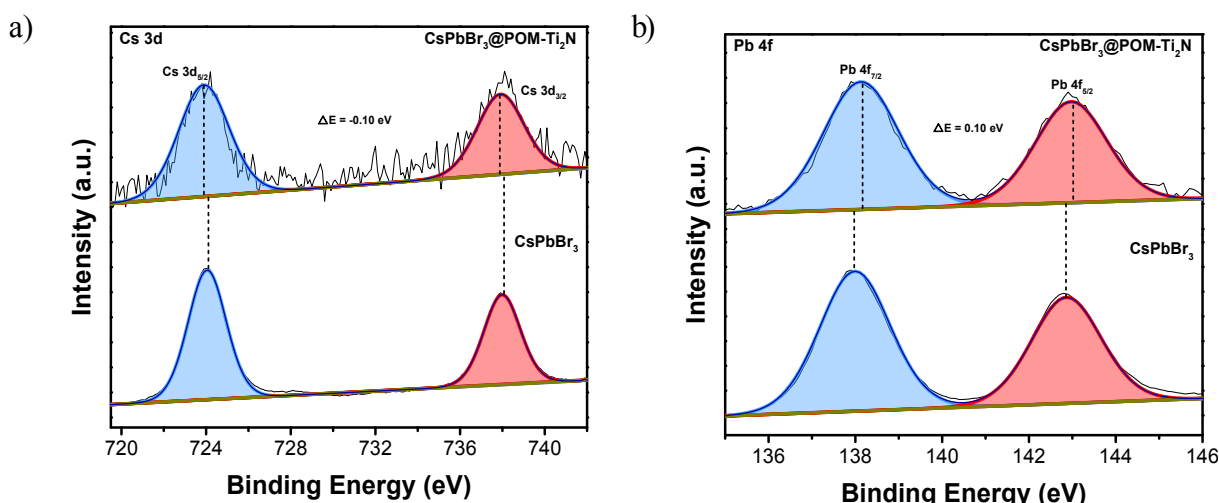


**Figure 4.** (a) Photoluminescence spectra ( $\lambda_{\text{ex}} = 405 \text{ nm}$ ) of  $\text{CsPbBr}_3$  nanoparticles (red line) and  $\text{CsPbBr}_3@\text{POM-Ti}_2\text{N}$  MXene catalyst (blue line). (b) Lifetime measurements registered at 530 and 513 nm under room conditions of  $\text{CsPbBr}_3$  nanoparticles (blue line) and  $\text{CsPbBr}_3@\text{POM-Ti}_2\text{N}$  MXene catalyst (red line) respectively. The PL decay lifetimes were calculated to the best fitting to a biexponential decay model ( $y = A_1 \cdot e^{-t/\tau_1} + A_2 \cdot e^{-t/\tau_2}$ ), where  $A_1$  and  $A_2$  correspond to the amplitudes and  $\tau_1$  and  $\tau_2$  is the lifetime of each component). The average lifetime was calculated using the formula:  $\tau_{\text{average}} = A_1 \cdot \tau_1^2 + A_2 \cdot \tau_2^2 / A_1 \cdot \tau_1 + A_2 \cdot \tau_2$ .

X-ray photoelectron spectroscopy (XPS) measurements were conducted to determine the chemical states of lead (Pb), bromine (Br), cesium (Cs), titanium (Ti), nitrogen (N) and oxygen (O) in the  $\text{CsPbBr}_3$  NCs, POM-Ti<sub>2</sub>N, and NCs@POM-Ti<sub>2</sub>N samples (Figures S12, S13, and S14 show the full survey scans). Figure S12 displays the XPS core spectra for Cs 3d, Pb 4f, and Br 3d states, respectively, calibrated using the adventitious C 1s peak set to a binding energy (BE) of 284.8 eV.<sup>40</sup> In the case of  $\text{CsPbBr}_3$  NCs, the BE peaks for Cs 3d at 724.0 and 738.0 eV correspond to the Cs 3d<sub>5/2</sub> and Cs 3d<sub>3/2</sub> signals (Figure 5a) while the Pb 4f spectrum shows two peaks at 138.0 and 142.9 eV, attributed to the Pb 4f<sub>7/2</sub> and Pb 4f<sub>5/2</sub> levels respectively, of the Pb<sup>2+</sup> state, consistent with previous literature reports.<sup>41,42</sup> (Figure 5b) Additionally, two Br 3d peaks are observed at 67.9 and 69.0 eV, corresponding to Br 3d<sub>5/2</sub> and Br 3d<sub>3/2</sub> contributions.<sup>43,44</sup> (Figure 5c) Further examination of the Ti 2p spectrum for the NCs@POM-Ti<sub>2</sub>N composite reveals that the Ti 2p<sub>3/2</sub> and Ti 2p<sub>1/2</sub> levels corresponding to Ti-N in POM-Ti<sub>2</sub>N appear at BE values of 458.5 and 464.2 eV, respectively. The Ti 2p<sub>3/2</sub> and Ti 2p<sub>1/2</sub> levels associated with Ti-

O bonds characterize the POM-Ti<sub>2</sub>N MXene, with various oxidation states from Ti<sup>2+</sup> to Ti<sup>4+</sup> presenting at BE values around 455.7 - 459.8 and 461 - 466 eV, respectively.<sup>45,46</sup> (Figure 5d) Further evidence of the formation of the composite NCs@POM-Ti<sub>2</sub>N is found in the XPS spectrum shown in Figure 5, which analyses the elemental XPS signals of CsPbBr<sub>3</sub> and POM-Ti<sub>2</sub>N MXene before and after formation of the composite. Due to the effective formation of an interface between perovskites and POM-Ti<sub>2</sub>N MXene, subtle shifts in the Pb, Br, Ti, and N peak positions are observed, as shown below. Specifically, the binding energies for Pb 4f and Br 3d in the NCs@POM-Ti<sub>2</sub>N composite shift towards more positive values, indicating a reduction in electron density on CsPbBr<sub>3</sub>.<sup>47</sup> Conversely, the binding energies assigned to Ti 2p and N 1s (from Ti-N bonding) exhibit a negative shift, suggesting an increase in electron density on the POM-Ti<sub>2</sub>N MXene particles (Figure 5d, e).<sup>48</sup> The Ti 2p spectrum of the NCs@POM-Ti<sub>2</sub>N composite shows a clear shift of the main peak positions to lower BE values compared to POM-Ti<sub>2</sub>N MXene alone, indicating a chemical interaction between the perovskite nanocrystals and the POM-Ti<sub>2</sub>N MXene structure.

In addition, despite partial oxidation of the nitride MXene, Ti-N bonds characteristic of titanium nitride predominates, as evidenced by Ti 2p<sub>3/2</sub> and Ti 2p<sub>1/2</sub> signals at binding energies of approximately 458.5 eV and 464.2 eV, respectively. Additionally, the presence of an N 1s signal around 399.5 eV confirms the continued existence of N-Ti bonds,<sup>49,50</sup> and the peak at 400.8 eV may be associated with nitrogen atoms in the Ti(N, O) oxynitride lattice. (Figure 5e) These findings indicate that, although some surface oxidation occurs, forming TiO<sub>2</sub>, the internal structure of POM-Ti<sub>2</sub>N predominantly retains its titanium-nitride bonds, thus facilitating an effective electronic interaction with the CsPbBr<sub>3</sub> nanocrystals. In summary, all these observations support the notion of electronic interaction between the orbitals that form CsPbBr<sub>3</sub> NCs and POM-Ti<sub>2</sub>N MXene.



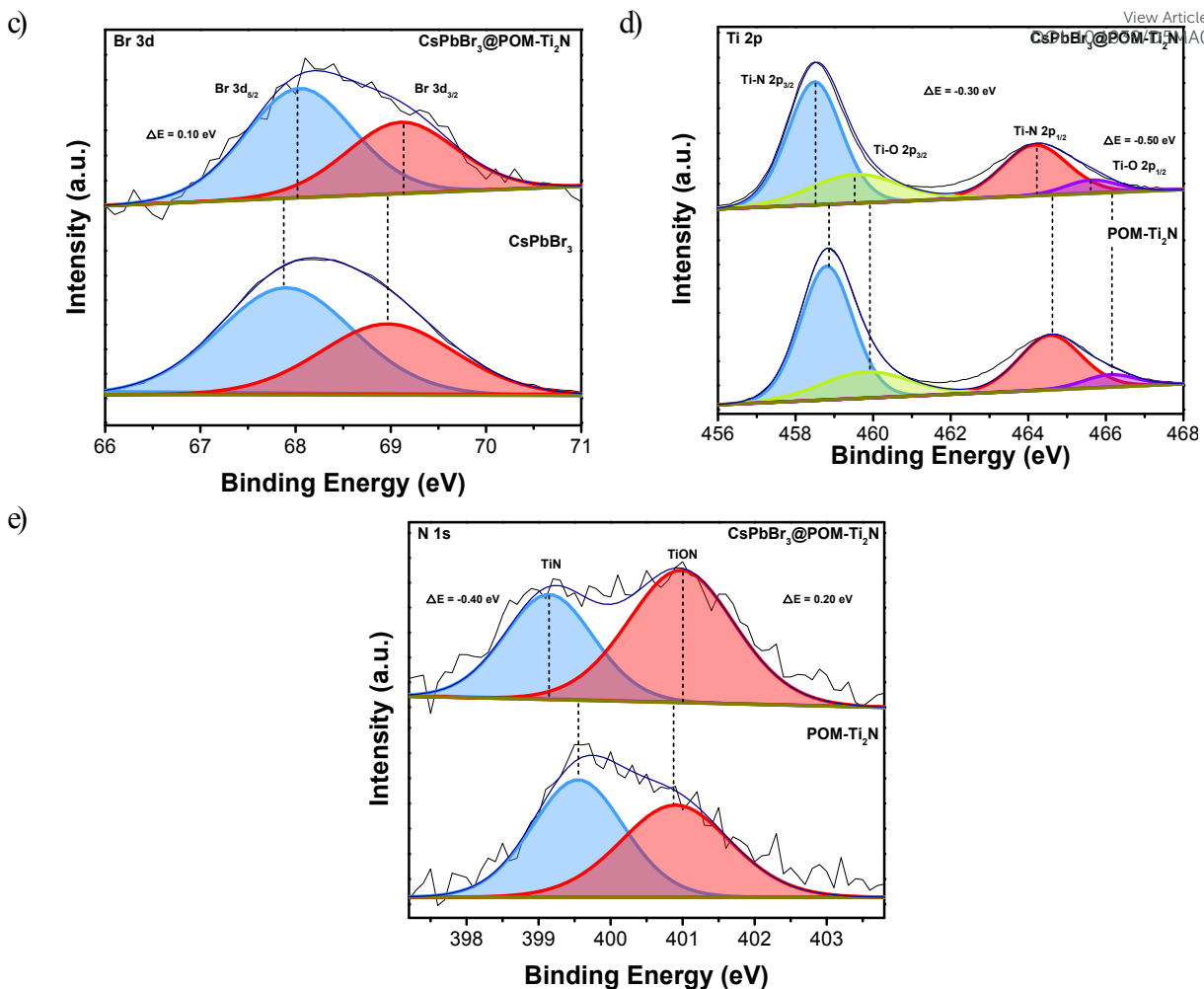


**Figure 5.** XPS spectra of CsPbBr<sub>3</sub> NCs, POM-Ti<sub>2</sub>N (below), and NCs@POM-Ti<sub>2</sub>N composites (top): a) Cs 3d spectra, b) Pb 4f spectra, c) Br 3d spectra, d) Ti 2p spectra, and e) N 1s spectra.

To investigate the reducibility and metal–support interactions within the hybrid, H<sub>2</sub> temperature-programmed reduction (H<sub>2</sub>-TPR) measurements were conducted (Figure 6a). Pure TiO<sub>2</sub> exhibits only a weak, broad reduction event centred at ~535 °C,<sup>51</sup> characteristic of kinetically hindered lattice-oxygen removal and indicative of strongly bound oxygen species with low surface mobility. A similar trend has been observed for TiO<sub>2</sub> nanosheets by other authors.<sup>52</sup> Conversely, the POM–Ti<sub>2</sub>N composite exhibits a markedly different H<sub>2</sub> consumption behavior, revealing two pronounced low-temperature reduction peaks with maxima centered at 314 °C and 381 °C. The presence of these features at significantly lower temperatures reflects the formation of highly labile surface oxygen species generated at the Ti<sub>2</sub>N/TiO<sub>2</sub> interface.<sup>53</sup> According to the reducibility criterion, where lower peak temperatures correspond to more weakly bonded oxygen species such as O<sup>−</sup>/O<sup>2−</sup>,<sup>54</sup> these events confirm the emergence of readily accessible active oxygen centres not present in pristine TiO<sub>2</sub>. This enhanced reducibility is attributed to a strong metal-support interaction (SMSI) between the almost conductive Ti<sub>2</sub>N

core and the ultrathin surface-oxidised  $\text{TiO}_2$  shell.<sup>55</sup> The  $\text{Ti}_2\text{N}$  framework promotes electron donation, activating  $\text{H}_2$  molecules and facilitating the formation of hydrides, which collectively weakens the surface Ti-O bonds and triggers stepwise reduction of the MXene surface. Concurrently, the high-temperature feature centred at  $\sim 530$  °C originates from the reduction of oxidised  $\text{TiO}_2$  moieties anchored on the POM surface, consistent with the consumption of more strongly bound lattice oxygen. Taken together, these redox characteristics demonstrate that the POM– $\text{Ti}_2\text{N}$  hybrid possesses substantially improved oxygen lability and electronic coupling compared to pristine  $\text{TiO}_2$ . Such behaviour is essential for catalytic activation, as the generation of easily reducible oxygen species and the formation of a robust  $\text{Ti}_2\text{N}$ – $\text{TiO}_2$  heterojunction provide the active environment required for efficient  $\text{H}_2$  dissociation,  $\text{CO}_2$  adsorption, and subsequent photothermal reduction to CO and  $\text{CH}_4$ .

Furthermore, the  $\text{CO}_2$  adsorption behaviour of POM– $\text{Ti}_2\text{N}$  and  $\text{TiO}_2$  was further examined by  $\text{CO}_2$  temperature-programmed desorption ( $\text{CO}_2$ -TPD), as illustrated in Figure 6b. POM– $\text{Ti}_2\text{N}$  and  $\text{TiO}_2$  exhibit a desorption peak in the low-temperature region ( $\sim 105$  °C),<sup>56</sup> which can be attributed to physisorbed  $\text{CO}_2$  weakly interacting with surface hydroxyl groups. In the case of  $\text{TiO}_2$ , this low-temperature feature dominates the profile, indicating a limited population of strongly adsorbed carbonate species.<sup>57</sup> In contrast, POM– $\text{Ti}_2\text{N}$  displays a markedly enhanced desorption signal extending into the high-temperature region (350 - 700 °C), with a pronounced maximum centred at approximately 525 °C. This peak reflects the formation of strongly bound carbonate species, resulting from the interaction of  $\text{CO}_2$  with basic surface sites generated during the formation of the  $\text{TiO}_2$  moieties within the POM– $\text{Ti}_2\text{N}$  heterostructure. The significantly increased desorption intensity suggests an enlarged density of active sites capable of stabilising chemisorbed  $\text{CO}_2$  species. These results collectively indicate that the incorporation of  $\text{Ti}_2\text{N}$  and its partial oxidation to  $\text{TiO}_2$  enhances both the strength and capacity of  $\text{CO}_2$  adsorption.

View Article Online  
DOI: 10.1039/DSMA01122A

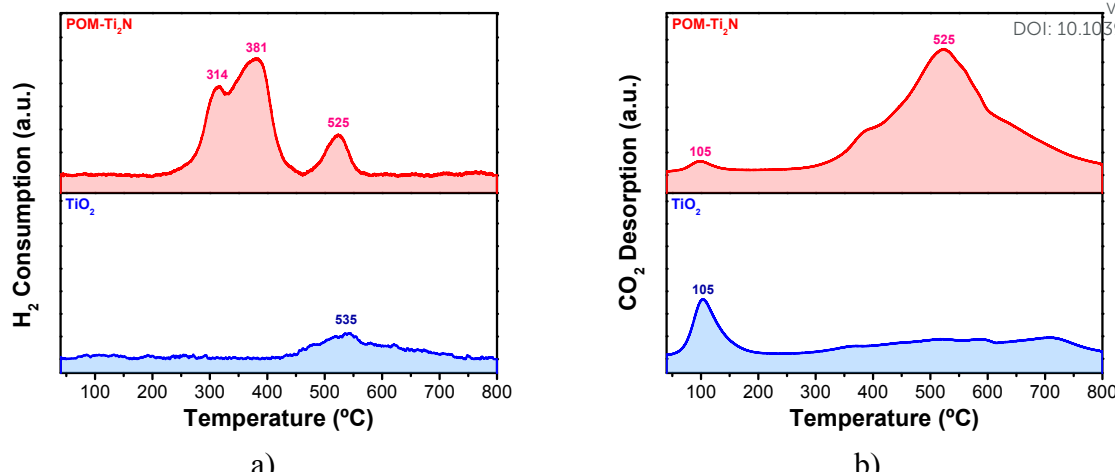


**Figure 6.** a) H<sub>2</sub>-TPR analysis profiles of the tested materials: POM-Ti<sub>2</sub>N (red line) and TiO<sub>2</sub> (blue line). b) CO<sub>2</sub>-TPD profiles obtained on POM-Ti<sub>2</sub>N (red line) and TiO<sub>2</sub> (blue line) materials. In both studies, the ramp rate was 10°C·min<sup>-1</sup>.

Periodic DFT calculations were performed with VASP (PAW-PBE including dispersion corrections,<sup>58,59</sup> full computational details are provided in the Supporting Information) on three representative Ti-based supports designed to mimic the POM-Ti<sub>2</sub>N composite: a Ti<sub>2</sub>N MXene monolayer (conductive nitride core), a rock-salt TiN(100) slab (nitride surface), and rutile TiO<sub>2</sub>(110) surfaces with and without a surface oxygen vacancy, V<sub>O</sub> (partially oxidized TiO<sub>2</sub>/TiO<sub>x</sub> domains) (Figure S15). CO<sub>2</sub> and H<sub>2</sub> were individually adsorbed at low coverage on each model, exploring several initial geometries. Among these, Ti<sub>2</sub>N exhibited the largest thermodynamic affinity for CO<sub>2</sub> ( $E_{ads} = -3.32$  eV),<sup>60,61</sup> whereas stoichiometric TiO<sub>2</sub>(110) bound CO<sub>2</sub> only weakly ( $E_{ads} = -0.10$  eV), in line with previous DFT and surface-science studies.<sup>62,63</sup> Introducing a surface oxygen vacancy on TiO<sub>2</sub>(110) markedly strengthened CO<sub>2</sub> adsorption ( $E_{ads} = -1.11$  eV) and led to bent, vacancy-anchored configurations, consistent with the enhanced reactivity of defective rutile surfaces.<sup>64–66</sup> In contrast, molecular H<sub>2</sub> adsorption was found to be very weak on all Ti-based supports ( $|E_{ads}(H_2)| \leq 0.05$  eV), while an artificially initialized, dissociated H<sub>2</sub> state on Ti<sub>2</sub>N was strongly stabilized ( $E_{ads} = -7.57$  eV per H<sub>2</sub>), indicating that nitride sites act as a deep thermodynamic sink for atomic hydrogen rather than as strong chemisorption sites for molecular H<sub>2</sub>.<sup>67</sup> Taken together with the H<sub>2</sub>-TPR and CO<sub>2</sub>-TPD data, these DFT trends support a bifunctional picture in which oxygen-deficient TiO<sub>2</sub>/TiO<sub>x</sub> regions and TiO<sub>2</sub>/Ti<sub>2</sub>N interfacial sites provide the main CO<sub>2</sub>-binding and activation centres, whereas the TiN/Ti<sub>2</sub>N scaffold supplies electronic/photothermal conductivity and preferentially stabilizes dissociated hydrogen species, as described in detail in the DFT analysis (see Supporting Information).

## Catalytic Activity of the NCs@POM-Ti<sub>2</sub>N material

View Article Online  
DOI: 10.1039/D5MA01122A

First, the catalytic activity of NCs@POM-Ti<sub>2</sub>N was studied in temperatures ranging between 160 to 250 °C, either in the dark (thermal catalysis) or under light irradiation (photo-thermal catalysis). Figures 7, S16 and S17 summarizes the catalytic results obtained under light and dark conditions. In both cases, under light or dark, at low temperatures selectivity towards CH<sub>4</sub> is 100% but as temperature increases selectivity shifts to CO. Additionally, maximum conversion is achieved above 200 °C whereas at 250 °C the activity drops. This fact can be due to changes happening on the support as the colour of POM-Ti<sub>2</sub>N shifted from light grey to dark grey at these temperatures. On the other hand, as shown in Figure 7, under light irradiation production of CO<sub>2</sub>-derived products is always higher compared to dark. These differences in the catalytic activity indicate that CO<sub>2</sub> conversion in NCs@POM-Ti<sub>2</sub>N light effectively assists the reaction.

A deeper analysis of catalytic data summarized in Table 1 brings further arguments for the photo-thermal catalytic pathway, especially, which is more evident at lower temperatures. A comparison of CO<sub>2</sub> conversion or CH<sub>4</sub> production at temperatures of 160 °C or 180 °C leads to conversions 5 to 4-fold higher when photo-thermal conditions are applied. Interestingly, both thermal and photothermal conditions share similar trends displaying higher conversions at 220 °C, in both cases, CO production starts at 200 °C and has a gaussian plot in which 220 °C seems to be the most active temperature conditions. It seems that at higher temperatures than 180 °C desorption of reaction intermediates is favored difficulty the complete hydrogenation of CO<sub>2</sub> to CH<sub>4</sub>.

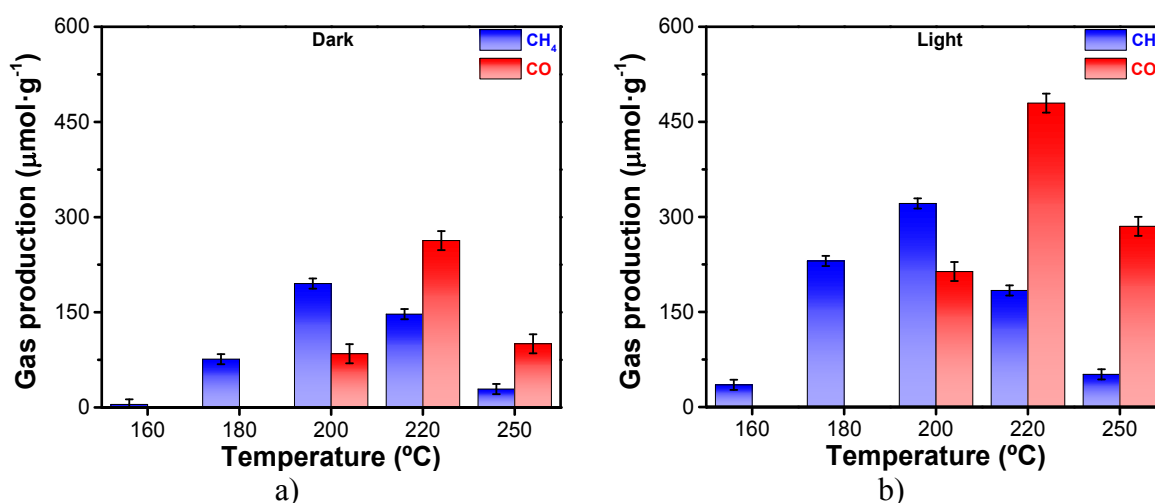


**Figure 7.** Photocatalytic activity for CsPbBr<sub>3</sub>(5 wt%)@POM-Ti<sub>2</sub>N MXene under different conditions of temperature (a) in the dark, (b) under light irradiation. Reaction conditions: CsPbBr<sub>3</sub>(5 wt%)@POM-Ti<sub>2</sub>N MXene (10mg), P<sub>H2</sub> = 1.2 bar, P<sub>CO2</sub> = 0.3 bar, at 23h reaction time, simulated sunlight irradiation (226 mW·cm<sup>-2</sup>), and temperature as indicated.

**Table 1.** Comparison of CH<sub>4</sub> and CO selectivity of CsPbBr<sub>3</sub>(5 wt %)@POM-Ti<sub>2</sub>N MXene at different temperatures and conditions (dark or light).

T. Reaction (°C)	Condition	Selectivity CH <sub>4</sub> (%)	Selectivity CO (%)
160	Dark	100	0
	Light	100	0
180	Dark	100	0
	Light	100	0
200	Dark	70	30
	Light	60	40
220	Dark	36	64
	Light	28	72
250	Dark	22	78
	Light	15	85

For comparison, we studied the photo-thermal activity for CO<sub>2</sub> reduction using CsPbBr<sub>3</sub> nanocrystals and CsPbBr<sub>3</sub>@POM-Ti<sub>2</sub>N MXene at 200°C. (Figure 8). As can be seen, our CsPbBr<sub>3</sub>@POM-Ti<sub>2</sub>N catalyst presents the highest activity for CH<sub>4</sub> production compared to pristine CsPbBr<sub>3</sub> NCs or POM-Ti<sub>2</sub>N MXene alone. In fact, while the components of the composite CsPbBr<sub>3</sub> and M- Ti<sub>2</sub>N MXene are not as active as the pristine POM- Ti<sub>2</sub>N we assume the catalytically active sites are present in the oxidized side of the POM- Ti<sub>2</sub>N. (Figure 8a) However, selectivity changes occurred when POM-Ti<sub>2</sub>N is loaded with the perovskite due to the suppression of CO production and a change of selectivity towards CH<sub>4</sub>. This indicates a synergistic effect between both materials when they form a combined material.

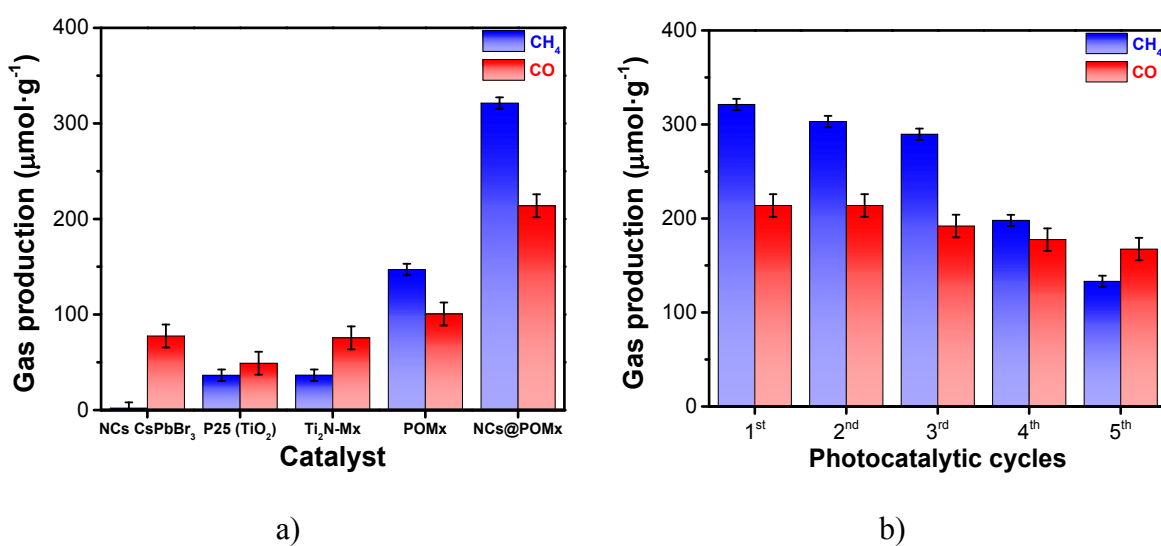


**Figure 8.** a) Comparison of photocatalytic activity for different samples. b) Recycling of the photocatalyst CsPbBr<sub>3</sub>(5 wt%)@POM-Ti<sub>2</sub>N MXene. Reaction conditions: Photocatalyst (10mg), P<sub>H2</sub> = 1.2 bar, P<sub>CO2</sub> = 0.3 bar, at 23h reaction time, simulated sunlight irradiation (226 mW·cm<sup>-2</sup>), and 200 °C.

In addition, the recyclability of  $\text{CsPbBr}_3@\text{POM-Ti}_2\text{N}$  MXene was evaluated over five consecutive cycles under identical reaction conditions, as illustrated in Figure 8b. The results indicate a stable  $\text{CH}_4$  production yield for the first three cycles (only a 3% reduction in activity per cycle), suggesting desirable photostability of the catalyst, even with each cycle lasting 23 hours. Interestingly, while  $\text{CH}_4$  remained the primary product, CO was observed as a byproduct of the reaction. We attribute this emergent CO formation to surface restructuring and the gradual alteration of active sites, likely due to subtle changes in the surface composition or morphology of the  $\text{CsPbBr}_3@\text{POM-Ti}_2\text{N}$  during the initial reaction cycle. This shift in selectivity, with CO generation emerging, may be explained by changes in the binding and activation of  $\text{CO}_2$  at newly exposed or modified active sites on the catalyst surface. This argument get reinforced since XPS data shown in Figure 5 reveals the electronic polarization in Cs and Ti atoms after the formation of  $\text{CsPbBr}_3@\text{POM-Ti}_2\text{N}$ , suggesting that perovskite NCs are not randomly deposited, if not interacting somehow. Photocatalytic  $\text{CO}_2$  reduction involves a series of complex, multi-step processes, including light absorption, charge separation, reactant adsorption, and catalytic reduction at active sites.<sup>68</sup> Minor modifications in any of these steps—particularly in the structure of surface-active sites can significantly impact product selectivity. In this case, MXene support likely plays a dual role: enhancing electron-hole separation and simultaneously protecting  $\text{CsPbBr}_3$  nanocrystals from rapid degradation, as confirmed by the absence of notable changes in XRD patterns (Figure 1, black line) and consistent XPS spectra. Nevertheless, with continued cycling, slight restructuring of the surface may expose new catalytic sites that favor CO production. By the fourth cycle, a reduction of approximately 30% in  $\text{CH}_4$  yield was observed, possibly due to gradual surface degradation or partial deactivation of active sites, while CO production remained stable. This indicates that, despite a decrease in  $\text{CH}_4$  yield, the modified surface continues to facilitate  $\text{CO}_2$  reduction to CO, suggesting persistent reactivity at specific catalytic sites that favor CO production over  $\text{CH}_4$ . In fact, while  $\text{CsPbBr}_3@\text{POM-Ti}_2\text{N}$  has higher selectivity towards  $\text{CH}_4$ , their individual components (M-Ti<sub>2</sub>N MXene, POM-Ti<sub>2</sub>N MXene, and  $\text{CsPbBr}_3$  nanocrystals) are also selective to CO. This change in catalytic activity agrees with superficial chemicophysical changes on POM-Ti<sub>2</sub>N surface. This matches with the observation made in the XPS in terms of electronic densities of atomic elements that compose  $\text{CsPbBr}_3$  NCs and the POM-Ti<sub>2</sub>N. These findings underscore the importance of optimizing both the initial surface properties and long-term stability of active sites to maintain selective  $\text{CO}_2$  photoreduction over extended reaction cycles.

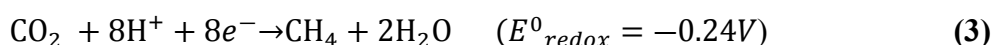
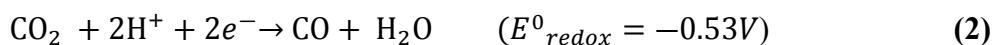
View Article Online  
DOI: 10.1039/D5MA01122A

## Proposed mechanism (Photocatalytic CO<sub>2</sub> Reduction)

According to XPS and UV-Vis measurements, the energy alignments of CB and VB of CsPbBr<sub>3</sub> NCs, POM-Ti<sub>2</sub>N, and CsPbBr<sub>3</sub>@POM-Ti<sub>2</sub>N were calculated. From a thermodynamic point of view, the reduction of CO<sub>2</sub> to CO and CH<sub>4</sub> in all cases, see Figure 9b. However, CO<sub>2</sub> conversion increases in a considerable way in the case of the CsPbBr<sub>3</sub>@POM-Ti<sub>2</sub>N composite, specially upon UV-Vis light exposure. This fact, plus the intrinsic heterojunction morphology of the composite (see Figure 9a) suggests that photogenerated electrons can flow from the conduction band (CB) of the perovskite to the CB of the TiO<sub>2</sub> layer that eventually will pass to the Ti<sub>2</sub>N. Thus, inducing effective charge separation enabled by a type II heterojunction formed between the CsPbBr<sub>3</sub> NCs and the POM-Ti<sub>2</sub>N MXene structure. Additionally, the difference in potential between the two materials generates an internal electric field (IEF) that further enhances charge separation and transfer efficiency.<sup>69</sup> The direction of the IEF may be proved by XPS results (Figure 5).

The TiO<sub>2</sub> layer also reduces direct recombination between the perovskite and the MXene, forming an additional small electric field that promotes electron flow into the MXene and avoids recombination. The introduction of such an interlayer to reduce direct recombination is a well-known strategy in the field of dye-sensitized solar cells (DSSCs) and hybrid solar cells.<sup>70,71</sup>

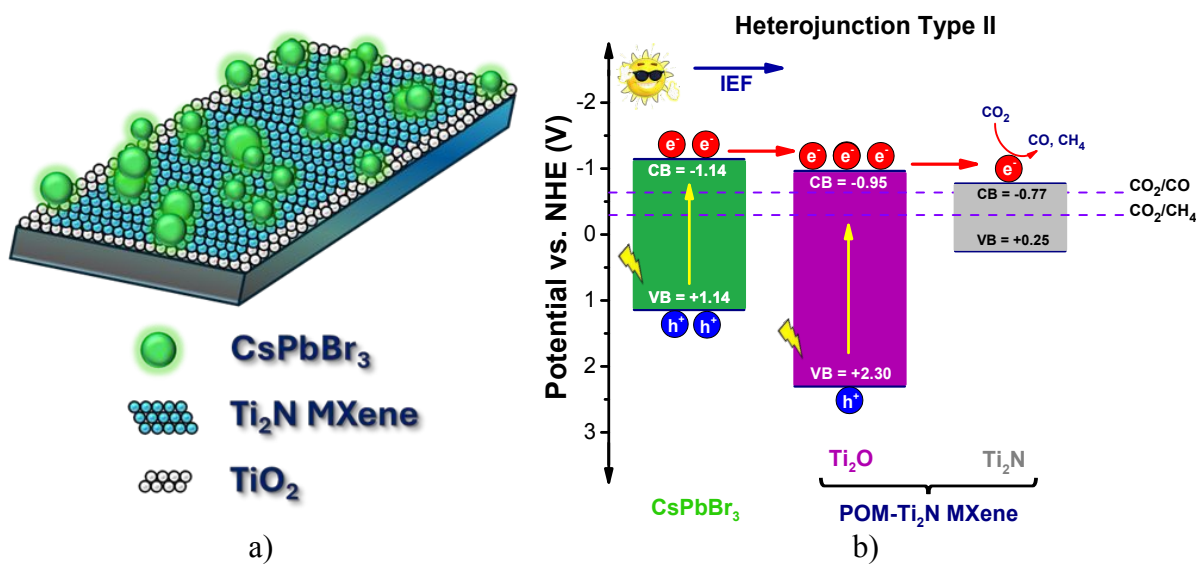
Thus, these electrons that are injected to the MXene can reduce CO<sub>2</sub> into either CO or CH<sub>4</sub> through multielectron transfer pathways:<sup>72</sup>



Moreover, these reactions proceed concurrently, with their predominance governed by the interplay between thermodynamic feasibility and kinetic accessibility. Thermodynamically, the formation of CH<sub>4</sub> is favored; however, kinetically, CO production is more accessible as it requires fewer electrons (2e<sup>-</sup> vs. 8e<sup>-</sup> for CH<sub>4</sub>). Experimental data from Table 1 and Figure 7 confirm this duality. At lower temperatures (160 - 180 °C), CH<sub>4</sub> selectivity remains at 100%, indicating a thermodynamically driven process. However, as the temperature increases (200 - 250 °C), a significant shift in selectivity toward CO is observed, dropping CH<sub>4</sub> selectivity to 15% under illumination at 250 °C. These results suggest that at higher reaction temperatures, kinetic factors increasingly govern product distribution.

Therefore, the temperature-dependent behavior observed in the CsPbBr<sub>3</sub>@POM-Ti<sub>2</sub>N composite under light irradiation illustrates a nuanced balance between thermodynamics and kinetics.<sup>73</sup>

In summary, the superior photocatalytic activity of  $\text{CsPbBr}_3$ @POM- $\text{Ti}_2\text{N}$  can be attributed to several synergistic factors. First, the composite exhibits enhanced light absorption across the visible spectrum compared to the individual components (Figure 8a), generating more charge carriers. Second, the heterojunction architecture suppresses electron-hole recombination, thereby ensuring greater availability of charge carriers for surface redox reactions. Lastly, the 2D/0D structural configuration—where zero-dimensional  $\text{CsPbBr}_3$  NCs are uniformly distributed over a two-dimensional layers of POM- $\text{Ti}_2\text{N}$  support—maximizes active surface area and facilitates efficient interfacial charge migration. (Figure 9)



1. Upon illumination, the perovskite absorbs photons, generating electron-hole pairs.
2. Internal electric fields (IEF) push electrons toward  $\text{TiO}_2$  and then to MXene.
3. Electrons accumulate at the MXene surface, where they reduce  $\text{CO}_2$  to  $\text{CO}$  and  $\text{CH}_4$ .

**Figure 9.** a) The schematic diagram of  $\text{CsPbBr}_3$ @POM- $\text{Ti}_2\text{N}$  composite. b) Diagram of  $\text{CH}_4$  and CO production by  $\text{CsPbBr}_3$ @POM- $\text{Ti}_2\text{N}$  composite system under sunlight irradiation and charge migration and separation.

### 3. Conclusions

In conclusion, this study highlights the successful synthesis and performance of a novel hybrid heterojunction composed of  $\text{CsPbBr}_3$  nanocrystals supported on partially oxidized  $\text{Ti}_2\text{N}$  MXenes (POM- $\text{Ti}_2\text{N}$ ), specifically engineered for efficient photo-thermal  $\text{CO}_2$  conversion into  $\text{CH}_4$  and CO. Preparation of the hybrid material was achieved through by simple ultrasonic impregnation, enabling the uniform deposition of  $\text{CsPbBr}_3$  NCs onto the surface of the 2D POM- $\text{Ti}_2\text{N}$  sheets. The partial oxidation of  $\text{Ti}_2\text{N}$  was fundamental to introducing oxygen-containing functional groups, which improved surface hydrophilicity and provided anchoring sites for the nanocrystals. This facilitated strong interfacial interactions, critical for enhancing the overall photocatalytic activity.

The proposed mechanism involves a synergistic interplay between light absorption, charge separation, thermodynamic, and kinetic effects.  $\text{CsPbBr}_3$  NCs serve as efficient light harvesters due to their strong absorption in the visible range and excellent charge transport properties. Upon irradiation, electron–hole pairs are generated in the perovskite, with electrons being efficiently transferred to the POM- $\text{Ti}_2\text{N}$  support. The partially oxidized MXene acts both as a photothermal catalyst and an electron sink, avoiding charge recombination to promote the catalytic reduction of  $\text{CO}_2$ , while simultaneously accelerating charge separation and transport. The presence of oxygen vacancies and various oxidation states from  $\text{Ti}^{2+}$  to  $\text{Ti}^{4+}$  on the POM- $\text{Ti}_2\text{N}$  surface further facilitates  $\text{CO}_2$  adsorption and activation, which are essential for driving the  $\text{CH}_4$  and CO formation pathway with high selectivity.

In terms of recyclability, the hybrid catalyst demonstrated excellent structural integrity, maintaining its catalytic activity over multiple reaction cycles. Post-reaction analyses showed minimal degradation of the  $\text{CsPbBr}_3$  NCs, retaining the interfacial architecture and confirming the robustness of the catalyst under operational conditions. Overall, the  $\text{CsPbBr}_3@\text{POM-}\text{Ti}_2\text{N}$  hybrid catalyst demonstrates a promising strategy for the design of stable and highly active photocatalysts, combining the tunable optoelectronic properties of perovskite NCs with the multifunctionality of 2D MXenes. The enhancement in  $\text{CH}_4$  and CO production under light-driven conditions underscores the potential of this hybrid catalyst in advancing solar-to-fuel technologies.

## Supporting Information

Additional supporting information can be found online in the Supporting Information section.

## Acknowledgements

This research was funded by the Spanish Ministry of Science and Innovation through MCIN/AEI/10.13039/501100011033/ and “FEDER a way of making Europe,” and the Severo Ochoa Centre of Excellence program (CEX2021-001230-S). K.M. acknowledges the PRE2022-104119 grant for the project "Catalytic processes: Catalysis for energy and process intensification by applying instrumental tools to monitor chemical processes." P.A. received funding from the PID2021-123163OB-I00 grant. H.G.B. was supported by the RYC2022-037287-I grant, PAID-06-23. Also, this research leading to these results has received funding from the European Union's Horizon Europe research and innovation programme (Project DAM4CO<sub>2</sub>, Double-Active Membranes for a sustainable CO<sub>2</sub> cycle; HORIZON-EIC-2022-000012).

PATHFINDERCHALLENGES-01-Number: 101115488). We thank the technical team at the [View Article Online](#)  
Instituto de Tecnología Química (ITQ) for their support in facilitating the characterizations.  
DOI: 10.1039/D5MA01122A

## References

- (1) Jiao, X.; Zheng, K.; Liang, L.; Li, X.; Sun, Y.; Xie, Y. Fundamentals and Challenges of Ultrathin 2D Photocatalysts in Boosting CO<sub>2</sub> Photoreduction. *Chem. Soc. Rev.* **2020**, *49* (18), 6592–6604. <https://doi.org/10.1039/D0CS00332H>.
- (2) Liao, G.; Ding, G.; Yang, B.; Li, C. Challenges in Photocatalytic Carbon Dioxide Reduction. *Precis. Chem.* **2024**, *2* (2), 49–56. [https://doi.org/10.1021/PRECHEM.3C00112/ASSET/IMAGES/LARGE/PC3C00112\\_0004.JPG](https://doi.org/10.1021/PRECHEM.3C00112/ASSET/IMAGES/LARGE/PC3C00112_0004.JPG).
- (3) Yu, J.; Muhetaer, A.; Li, Q.; Xu, D. Solar Energy-Driven Reverse Water Gas Shift Reaction: Photothermal Effect, Photoelectric Activation and Selectivity Regulation. *Small* **2024**, *20* (42), 2402952. <https://doi.org/10.1002/SMLL.202402952>.
- (4) Zhang, Y.; Ma, L.; Wang, T.; Li, X. MnO<sub>2</sub> Coated Fe<sub>2</sub>O<sub>3</sub> Spindles Designed for Production of C<sub>5+</sub> Hydrocarbons in Fischer–Tropsch Synthesis. *Fuel* **2016**, *177*, 197–205. <https://doi.org/10.1016/J.FUEL.2016.03.023>.
- (5) Liu, P.; Huang, Z.; Gao, X.; Hong, X.; Zhu, J.; Wang, G.; Wu, Y.; Zeng, J.; Zheng, X. Synergy between Palladium Single Atoms and Nanoparticles via Hydrogen Spillover for Enhancing CO<sub>2</sub> Photoreduction to CH<sub>4</sub>. *Adv. Mater.* **2022**, *34* (16), 2200057. <https://doi.org/10.1002/ADMA.202200057>.
- (6) Ridzuan, N. D. M.; Shaharun, M. S.; Anawar, M. A.; Ud-Din, I. Ni-Based Catalyst for Carbon Dioxide Methanation: A Review on Performance and Progress. *Catal.* **2022**, *Vol. 12, Page 469* **2022**, *12* (5), 469. <https://doi.org/10.3390/CATAL12050469>.
- (7) Carenco, S.; Tuxen, A.; Chintapalli, M.; Pach, E.; Escudero, C.; Ewers, T. D.; Jiang, P.; Borondics, F.; Thornton, G.; Alivisatos, A. P.; Bluhm, H.; Guo, J.; Salmeron, M. Dealloying of Cobalt from CuCo Nanoparticles under Syngas Exposure. *J. Phys. Chem. C* **2013**, *117* (12), 6259–6266. [https://doi.org/10.1021/JP4000297/SUPPL\\_FILE/JP4000297\\_SI\\_001.PDF](https://doi.org/10.1021/JP4000297/SUPPL_FILE/JP4000297_SI_001.PDF).
- (8) Xiao, S.; Wang, L.; Tang, Y.; Yang, Z.; Wang, H.; Guo, C.; Zhao, T.; Jiang, Y.; Wen, X.; Wang, F. Interfacial Structure Engineering Enhances Photo-Thermal CO<sub>2</sub> Hydrogenation over Ni-CeO<sub>2</sub> Nanocomposites. *Chem Catal.* **2025**, *5* (7), 101361. <https://doi.org/10.1016/J.CHECAT.2025.101361>.
- (9) Tang, Y.; Wang, H.; Guo, C.; Wang, L.; Zhao, T.; Xiao, S.; Liu, J.; Jiang, Y.; Zhao, Y.; Wen, X. D.; Wang, F. Synergies Between Atomically Dispersed Ru Single Atoms and Nanoparticles on CeAlO<sub>x</sub> for Enhanced Photo-Thermal Catalytic CO<sub>2</sub> Hydrogenation. *Adv. Mater.* **2025**, e12793.



<https://doi.org/10.1002/ADMA.202512793>; PAGE:STRING:ARTICLE/CHAPTER View Article Online  
DOI: 10.1039/D5MA01122A

(10) Li, X.; Wang, C.; Tang, J. Methane Transformation by Photocatalysis. *Nat. Rev. Mater.* 2022 **7** (8), 617–632. <https://doi.org/10.1038/s41578-022-00422-3>.

(11) Luo, T.; Gilmanova, L.; Kaskel, S. Advances of MOFs and COFs for Photocatalytic CO<sub>2</sub> Reduction, H<sub>2</sub> Evolution and Organic Redox Transformations. *Coord. Chem. Rev.* 2023, **490**, 215210. <https://doi.org/10.1016/J.CCR.2023.215210>.

(12) Wang, P.; Yang, F.; Qu, J.; Cai, Y.; Yang, X.; Li, C. M.; Hu, J. Recent Advances and Challenges in Efficient Selective Photocatalytic CO<sub>2</sub> Methanation. *Small* 2024, **20** (32), 2400700. <https://doi.org/10.1002/SMLL.202400700>.

(13) Shang, Z.; Feng, X.; Chen, G.; Qin, R.; Han, Y. Recent Advances on Single-Atom Catalysts for Photocatalytic CO<sub>2</sub> Reduction. *Small* 2023, **19** (48), 2304975. <https://doi.org/10.1002/SMLL.202304975>.

(14) Ullah, S.; Wang, J.; Yang, P.; Liu, L.; Yang, S. E.; Xia, T.; Guo, H.; Chen, Y. All-Inorganic CsPbBr<sub>3</sub> Perovskite: A Promising Choice for Photovoltaics. *Mater. Adv.* 2021, **2** (2), 646–683. <https://doi.org/10.1039/D0MA00866D>.

(15) Chen, Y. H.; Ye, J. K.; Chang, Y. J.; Liu, T. W.; Chuang, Y. H.; Liu, W. R.; Liu, S. H.; Pu, Y. C. Mechanisms behind Photocatalytic CO<sub>2</sub> Reduction by CsPbBr<sub>3</sub> Perovskite-Graphene-Based Nanoheterostructures. *Appl. Catal. B Environ.* 2021, **284**, 119751. <https://doi.org/10.1016/J.APCATB.2020.119751>.

(16) Wang, X.; He, J.; Chen, X.; Ma, B.; Zhu, M. Metal Halide Perovskites for Photocatalytic CO<sub>2</sub> Reduction: An Overview and Prospects. *Coord. Chem. Rev.* 2023, **482**, 215076.

(17) Li, X.; Liu, J.; Jiang, G.; Lin, X.; Wang, J.; Li, Z. Self-Supported CsPbBr<sub>3</sub>/Ti<sub>3</sub>C<sub>2</sub>T<sub>x</sub> MXene Aerogels towards Efficient Photocatalytic CO<sub>2</sub> Reduction. *J. Colloid Interface Sci.* 2023, **643**, 174–182. <https://doi.org/10.1016/J.JCIS.2023.04.015>.

(18) Pazniak, H.; Plugin, I. A.; Loes, M. J.; Inerbaev, T. M.; Burmistrov, I. N.; Gorshenkov, M.; Polcak, J.; Varezhnikov, A. S.; Sommer, M.; Kuznetsov, D. V.; Bruns, M.; Fedorov, F. S.; Vorobeva, N. S.; Sinitskii, A.; Sysoev, V. V. Partially Oxidized Ti<sub>3</sub>C<sub>2</sub>T<sub>x</sub> MXenes for Fast and Selective Detection of Organic Vapors at Part-per-Million Concentrations. *ACS Appl. Nano Mater.* 2020, **3** (4), 3195–3204. [https://doi.org/10.1021/ACSANM.9B02223/ASSET/IMAGES/MEDIUM/AN9B02223\\_M001.GIF](https://doi.org/10.1021/ACSANM.9B02223/ASSET/IMAGES/MEDIUM/AN9B02223_M001.GIF).

(19) Wang, H.; Peng, R.; Hood, Z. D.; Naguib, M.; Adhikari, S. P.; Wu, Z. Titania Composites with 2 D Transition Metal Carbides as Photocatalysts for Hydrogen

Production under Visible-Light Irradiation. *ChemSusChem* **2016**, *9* (12), 1490–1497. New Article Online DOI: 10.1039/D5MA01122A  
<https://doi.org/10.1002/CSSC.201600165>.

(20) Vighnesh, K.; Wang, S.; Liu, H.; Rogach, A. L. Hot-Injection Synthesis Protocol for Green-Emitting Cesium Lead Bromide Perovskite Nanocrystals. *ACS Nano* **2022**, *16* (12), 19618–19625.  
[https://doi.org/10.1021/ACSNANO.2C11689/ASSET/IMAGES/LARGE/NN2C11689\\_0004.JPG](https://doi.org/10.1021/ACSNANO.2C11689/ASSET/IMAGES/LARGE/NN2C11689_0004.JPG).

(21) Liu, X.; Li, Y.; Ding, H.; Chen, L.; Du, S.; Chai, Z.; Huang, Q. Topotactic Transition of Ti<sub>4</sub>AlN<sub>3</sub> MAX Phase in Lewis Acid Molten Salt. *J. Mater.* **2023**, *9* (6), 1032–1038.  
<https://doi.org/10.1016/J.JMAT.2023.03.012>.

(22) Wang, W. B.; Zhong, X.; He, Z. Y.; Wang, Z. X.; Zhang, P. Z. Plasma Niobium Surface Alloying of Pure Titanium and Its Oxidation at 900 °C. *Chinese J. Aeronaut.* **2007**, *20* (2), 111–114. [https://doi.org/10.1016/S1000-9361\(07\)60015-6](https://doi.org/10.1016/S1000-9361(07)60015-6).

(23) Lai, H. E.; Yoo, R. M. S.; Djire, A.; Balbuena, P. B. Investigation of the Vibrational Properties of 2D Titanium Nitride MXene Using DFT. *J. Phys. Chem. C* **2024**, *128* (8), 3327–3342.  
[https://doi.org/10.1021/ACS.JPCC.3C06717/ASSET/IMAGES/LARGE/JP3C06717\\_0012.JPG](https://doi.org/10.1021/ACS.JPCC.3C06717/ASSET/IMAGES/LARGE/JP3C06717_0012.JPG).

(24) Balvanz, A.; Bayikadi, K. S.; Liu, Z.; Ie, T. S.; Peters, J. A.; Kanatzidis, M. G. Unveiling the Monoclinic Phase in CsPbBr<sub>3</sub>-XCl<sub>x</sub> Perovskite Crystals, Phase Transition Suppression and High Energy Resolution  $\gamma$ -Ray Detection. *J. Am. Chem. Soc.* **2024**, *146*, 31836–31848.  
[https://doi.org/10.1021/JACS.4C10872/ASSET/IMAGES/LARGE/JA4C10872\\_0006.JPG](https://doi.org/10.1021/JACS.4C10872/ASSET/IMAGES/LARGE/JA4C10872_0006.JPG).

(25) Casanova-Chafer, J.; Garcia-Aboal, R.; Mego, K.; Malik, S. B.; Atienzar, P.; Llobet, E. Lead-Free Perovskite Nanocrystals Decorating Graphene for Detecting Nerve Agents. *ACS Appl. Electron. Mater.* **2024**, *6* (9), 6974–6981.  
[https://doi.org/10.1021/ACSAELM.4C01220/SUPPL\\_FILE/EL4C01220\\_SI\\_001.PDF](https://doi.org/10.1021/ACSAELM.4C01220/SUPPL_FILE/EL4C01220_SI_001.PDF).

(26) Low, J.; Zhang, L.; Tong, T.; Shen, B.; Yu, J. TiO<sub>2</sub>/MXene Ti<sub>3</sub>C<sub>2</sub> Composite with Excellent Photocatalytic CO<sub>2</sub> Reduction Activity. *J. Catal.* **2018**, *361*, 255–266.  
<https://doi.org/10.1016/J.JCAT.2018.03.009>.

(27) Akhtar, S.; Roy, S.; Tran, T. T.; Singh, J.; Sharbirin, A. S.; Kim, J. Low Temperature Step Annealing Synthesis of the Ti<sub>2</sub>AlN MAX Phase to Fabricate MXene Quantum Dots. *Appl. Sci.* **2022**, *Vol. 12, Page 4154* **2022**, *12* (9), 4154.



<https://doi.org/10.3390/APP12094154>.

View Article Online  
DOI: 10.1039/D5MA01122A

(28) Sharbirin, A. S.; Roy, S.; Tran, T. T.; Akhtar, S.; Singh, J.; Duong, D. L.; Kim, J. Light-Emitting Ti<sub>2</sub>N (MXene) Quantum Dots: Synthesis, Characterization and Theoretical Calculations. *J. Mater. Chem. C* **2022**, *10* (16), 6508–6514. <https://doi.org/10.1039/D2TC00568A>.

(29) Mandal, P.; Roy, A.; Mannar, S.; Viswanatha, R. Growth Mechanistic Insights into Perovskite Nanocrystals: Dimensional Growth. *Nanoscale Adv.* **2020**, *2* (11), 5305–5311. <https://doi.org/10.1039/D0NA00732C>.

(30) Mabhouti, K.; Norouzzadeh, P.; Taleb-Abbasi, M. Effects of Fe, Co, or Ni Substitution for Mn on La<sub>0.7</sub>Sr<sub>0.3</sub>MnO<sub>3</sub> Perovskite: Structural, Morphological, and Optical Analyses. *J. Non. Cryst. Solids* **2023**, *610*, 122283. <https://doi.org/10.1016/J.JNONCYSOL.2023.122283>.

(31) Saleem, M. I.; Yang, S.; Sulaman, M.; Hu, J.; Chandrasekar, P. V.; Shi, Y.; Zhi, R.; Batool, A.; Zou, B. All-Solution-Processed UV-IR Broadband Trilayer Photodetectors with CsPbBr<sub>3</sub> Colloidal Nanocrystals as Carriers-Extracting Layer. *Nanotechnology* **2020**, *31* (16), 165502. <https://doi.org/10.1088/1361-6528/AB667B>.

(32) Chacón-García, A. J.; Baldovi, H. G.; Babaryk, A. A.; Rodríguez-Díéguez, A.; Navalón, S.; Pérez, Y.; García, H.; Horcajada, P. Robust Hybrid Bismuth Perovskites as Potential Photocatalysts for Overall Water Splitting. *Nano Res.* **2024**, *17* (5), 4593–4601. <https://doi.org/10.1007/S12274-023-6254-1/METRICS>.

(33) Salcedo-Abraira, P.; Serrano-Nieto, R.; Biglione, C.; Cabrero-Antonino, M.; Vilela, S. M. F.; Babaryk, A. A.; Tilve-Martínez, D.; Rodriguez-Díéguez, A.; Navalón, S.; García, H.; Horcajada, P. Two Cu-Based Phosphonate Metal-Organic Frameworks as Efficient Water-Splitting Photocatalysts. *Chem. Mater.* **2023**, *35* (11), 4211–4219. [https://doi.org/10.1021/ACS.CHEMMATER.3C00054/SUPPL\\_FILE/CM3C00054\\_SI\\_003.CIF](https://doi.org/10.1021/ACS.CHEMMATER.3C00054/SUPPL_FILE/CM3C00054_SI_003.CIF).

(34) Mego, K.; Ruiz-Campos, P.; Baldoví, H. G.; Atienzar, P. OER Activity Promoted by Organic Ligand-Free Cs<sub>2</sub>Pt(Cl, Br)<sub>6</sub> Perovskite Photocatalyst for Solar-Driven Water Splitting. *Adv. Energy Sustain. Res.* **2025**, 2500105. <https://doi.org/10.1002/AESR.202500105>.

(35) Pan, A.; Ma, X.; Huang, S.; Wu, Y.; Jia, M.; Shi, Y.; Liu, Y.; Wangyang, P.; He, L.; Liu, Y. CsPbBr<sub>3</sub> Perovskite Nanocrystal Grown on MXene Nanosheets for Enhanced Photoelectric Detection and Photocatalytic CO<sub>2</sub> Reduction. *J. Phys. Chem. Lett.* **2019**, *10* (21), 6590–6597. <https://doi.org/10.1021/acs.jpclett.9b02605>.



(36) Tang, X.; Zu, Z.; Zang, Z.; Hu, Z.; Hu, W.; Yao, Z.; Chen, W.; Li, S.; Han, S.; Zhou, M. CsPbBr<sub>3</sub>/Reduced Graphene Oxide Nanocomposites and Their Enhanced Photoelectric Detection Application. *Sensors Actuators B Chem.* **2017**, *245*, 435–440. <https://doi.org/10.1016/J.SNB.2017.01.168>.

(37) Casanova-Chafer, J.; Garcia-Aboal, R.; Llobet, E.; Atienzar, P. Enhanced CO<sub>2</sub> Sensing by Oxygen Plasma-Treated Perovskite-Graphene Nanocomposites. *ACS Sensors* **2024**, *9* (2), 830–839. [https://doi.org/10.1021/ACSSENSORS.3C02166/ASSET/IMAGES/LARGE/SE3C02166\\_0008.JPG](https://doi.org/10.1021/ACSSENSORS.3C02166/ASSET/IMAGES/LARGE/SE3C02166_0008.JPG).

(38) Peters, J. A.; Liu, Z.; Yu, R.; McCall, K. M.; He, Y.; Kanatzidis, M. G.; Wessels, B. W. Carrier Recombination Mechanism in CsPbB R3 Revealed by Time-Resolved Photoluminescence Spectroscopy. *Phys. Rev. B* **2019**, *100* (23), 235305. <https://doi.org/10.1103/PHYSREVB.100.235305/FIGURES/6/MEDIUM>.

(39) Maduwanthi, C.; Jong, C. A.; Mohammed, W. S.; Hsu, S. H. Stability and Photocurrent Enhancement of Photodetectors by Using Core/Shell Structured CsPbBr<sub>3</sub>/TiO<sub>2</sub> Quantum Dots and 2D Materials. *Nanoscale Adv.* **2024**, *6* (9), 2328–2336. <https://doi.org/10.1039/D3NA01129A>.

(40) Fang, D.; He, F.; Xie, J.; Xue, L. Calibration of Binding Energy Positions with C1s for XPS Results. *J. Wuhan Univ. Technol. Mater. Sci. Ed.* **2020**, *35* (4), 711–718. <https://doi.org/10.1007/S11595-020-2312-7/METRICS>.

(41) Li, M.; Zhang, X.; Matras-Postolek, K.; Chen, H. S.; Yang, P. An Anion-Driven Sn<sup>2+</sup> Exchange Reaction in CsPbBr<sub>3</sub> Nanocrystals towards Tunable and High Photoluminescence. *J. Mater. Chem. C* **2018**, *6* (20), 5506–5513. <https://doi.org/10.1039/C8TC00990B>.

(42) Liu, X.; Ren, S.; Li, Z.; Guo, J.; Yi, S.; Yang, Z.; Hao, W.; Li, R.; Zhao, J. Flexible Transparent High-Efficiency Photoelectric Perovskite Resistive Switching Memory. *Adv. Funct. Mater.* **2022**, *32* (38), 2202951. <https://doi.org/10.1002/ADFM.202202951>.

(43) Pandey, P.; Sengupta, A.; Parmar, S.; Bansode, U.; Gosavi, S.; Swarnkar, A.; Muduli, S.; Mohite, A. D.; Ogale, S. CsPbBr<sub>3</sub>-Ti<sub>3</sub>C<sub>2</sub>T x MXene QD/QD Heterojunction: Photoluminescence Quenching, Charge Transfer, and Cd Ion Sensing Application. *ACS Appl. Nano Mater.* **2020**, *3* (4), 3305–3314. [https://doi.org/10.1021/ACSANM.0C00051/SUPPL\\_FILE/AN0C00051\\_SI\\_001.PDF](https://doi.org/10.1021/ACSANM.0C00051/SUPPL_FILE/AN0C00051_SI_001.PDF).

(44) Di, X.; Shen, L.; Jiang, J.; He, M.; Cheng, Y.; Zhou, L.; Liang, X.; Xiang, W. Efficient White LEDs with Bright Green-Emitting CsPbBr<sub>3</sub> Perovskite Nanocrystal in

View Article Online  
DOI: 10.1039/D5MA01122A

Mesoporous Silica Nanoparticles. *J. Alloys Compd.* **2017**, *729*, 526–532. [View Article Online](https://doi.org/10.1016/J.JALCOM.2017.09.213)  
[DOI: 10.1016/J.JALCOM.2017.09.213](https://doi.org/10.1016/J.JALCOM.2017.09.213)

(45) Halim, J.; Lukatskaya, M. R.; Cook, K. M.; Lu, J.; Smith, C. R.; Näslund, L. Å.; May, S. J.; Hultman, L.; Gogotsi, Y.; Eklund, P.; Barsoum, M. W. Transparent Conductive Two-Dimensional Titanium Carbide Epitaxial Thin Films. *Chem. Mater.* **2014**, *26* (7), 2374–2381.  
[https://doi.org/10.1021/CM500641A/SUPPL\\_FILE/CM500641A\\_SI\\_001.PDF](https://doi.org/10.1021/CM500641A/SUPPL_FILE/CM500641A_SI_001.PDF).

(46) Halim, J.; Cook, K. M.; Naguib, M.; Eklund, P.; Gogotsi, Y.; Rosen, J.; Barsoum, M. W. X-Ray Photoelectron Spectroscopy of Select Multi-Layered Transition Metal Carbides (MXenes). *Appl. Surf. Sci.* **2016**, *362*, 406–417.  
<https://doi.org/10.1016/J.APSUSC.2015.11.089>.

(47) Cheng, C.; He, B.; Fan, J.; Cheng, B.; Cao, S.; Yu, J. An Inorganic/Organic S-Scheme Heterojunction H<sub>2</sub>-Production Photocatalyst and Its Charge Transfer Mechanism. *Adv. Mater.* **2021**, *33* (22), 2100317. <https://doi.org/10.1002/ADMA.202100317>.

(48) Tang, Q.; Sun, Z.; Deng, S.; Wang, H.; Wu, Z. Decorating G-C<sub>3</sub>N<sub>4</sub> with Alkalized Ti<sub>3</sub>C<sub>2</sub> MXene for Promoted Photocatalytic CO<sub>2</sub> Reduction Performance. *J. Colloid Interface Sci.* **2020**, *564*, 406–417. <https://doi.org/10.1016/J.JCIS.2019.12.091>.

(49) Liuhe, L.; Lifang, X.; Xinxin, M. XPS of Ti+TiN+(N,C) Multilayer Films Deposited by Filtered Cathodic Arc Deposition with Controlled Feed Gas Flow Rate. *Surf. Coatings Technol.* **1999**, *120–121*, 618–621. [https://doi.org/10.1016/S0257-8972\(99\)00426-0](https://doi.org/10.1016/S0257-8972(99)00426-0).

(50) Coyac, D. C.; Kabachkov, E.; Kurkin, E.; Vershinin, N.; Balikhin, I.; Berestenko, V.; Michtchenko, A.; Shulga, Y.; Coyac, D. C.; Kabachkov, E.; Kurkin, E.; Vershinin, N.; Balikhin, I.; Berestenko, V.; Michtchenko, A.; Shulga, Y. Pt Supported on Plasma-Chemical Titanium Nitride for Efficient Room-Temperature CO Oxidation. *Mod. Res. Catal.* **2022**, *11* (1), 1–11. <https://doi.org/10.4236/MRC.2022.111001>.

(51) Zhu, H.; Qin, Z.; Shan, W.; Shen, W.; Wang, J. Pd/CeO<sub>2</sub>–TiO<sub>2</sub> Catalyst for CO Oxidation at Low Temperature: A TPR Study with H<sub>2</sub> and CO as Reducing Agents. *J. Catal.* **2004**, *225* (2), 267–277. <https://doi.org/10.1016/J.JCAT.2004.04.006>.

(52) Guo, C.; Wang, L.; Tang, Y.; Yang, Z.; Zhao, Y.; Jiang, Y.; Wen, X.; Wang, F. Enhanced Photo-Thermal CO<sub>2</sub> Methanation with Tunable R<sub>x</sub>Ni<sub>1-x</sub> Catalytic Sites: Alloying Beyond Pure Ru. *Adv. Funct. Mater.* **2025**, *35* (6), 2414931.  
<https://doi.org/10.1002/adfm.202414931>.

(53) Wang, J.; Vikrant, K.; Younis, S. A.; Kim, K. H.; Heynderickx, P. M. Low-



Temperature Oxidative Removal of Benzene from the Air Using Titanium Carbide (MXene)-Supported Platinum Catalysts. *Chemosphere* **2024**, *350*, 141114. [View Article Online](https://doi.org/10.1039/D5MA01122A) [DOI: 10.1039/D5MA01122A](https://doi.org/10.1039/D5MA01122A)

<https://doi.org/10.1016/J.CHEMOSPHERE.2024.141114>.

(54) Panov, G. I.; Dubkov, K. A.; Starokon, E. V. Active Oxygen in Selective Oxidation Catalysis. *Catal. Today* **2006**, *117* (1–3), 148–155. <https://doi.org/10.1016/J.CATTOD.2006.05.019>.

(55) Akalework, N. G.; Pan, C. J.; Su, W. N.; Rick, J.; Tsai, M. C.; Lee, J. F.; Lin, J. M.; Tsai, L. D.; Hwang, B. J. Ultrathin TiO<sub>2</sub>-Coated MWCNTs with Excellent Conductivity and SMSI Nature as Pt Catalyst Support for Oxygen Reduction Reaction in PEMFCs. *J. Mater. Chem.* **2012**, *22* (39), 20977–20985. <https://doi.org/10.1039/C2JM34361D>.

(56) Tang, Y.; Wang, H.; Guo, C.; Yang, Z.; Zhao, T.; Liu, J.; Jiang, Y.; Wang, W.; Zhang, Q.; Wu, D.; Zhao, Y.; Wen, X. D.; Wang, F. Ruthenium–Cobalt Solid-Solution Alloy Nanoparticles for Enhanced Photopromoted Thermocatalytic CO<sub>2</sub> Hydrogenation to Methane. *ACS Nano* **2024**, *18* (17), 11449–11461. <https://doi.org/10.1021/ACSNANO.4C02416>.

(57) Wan Isahak, W. N. R.; Che Ramli, Z. A.; Mohamed Hisham, M. W.; Yarmo, M. A. The Formation of a Series of Carbonates from Carbon Dioxide: Capturing and Utilisation. *Renew. Sustain. Energy Rev.* **2015**, *47*, 93–106. <https://doi.org/10.1016/J.RSER.2015.03.020>.

(58) Grimme, S.; Antony, J.; Ehrlich, S.; Krieg, H. A Consistent and Accurate Ab Initio Parametrization of Density Functional Dispersion Correction (DFT-D) for the 94 Elements H–Pu. *J. Chem. Phys.* **2010**, *132* (15), 154104. <https://doi.org/10.1063/1.3382344/926936>.

(59) Grimme, S.; Ehrlich, S.; Goerigk, L. Effect of the Damping Function in Dispersion Corrected Density Functional Theory. *J. Comput. Chem.* **2011**, *32* (7), 1456–1465. <https://doi.org/10.1002/JCC.21759>; JOURNAL:JOURNAL:1096987X;WGROUSTRING:PUBLICATION.

(60) Jurado, A.; Ibarra, K.; Morales-García, Á.; Viñes, F.; Illas, F. Adsorption and Activation of CO<sub>2</sub> on Nitride MXenes: Composition, Temperature, and Pressure Effects. *ChemPhysChem* **2021**, *22* (23), 2456–2463. <https://doi.org/10.1002/CPHC.202100600>; REQUESTEDJOURNAL:JOURNAL:14397641; PAGEGROUP:STRING:PUBLICATION.

(61) Morales-Salvador, R.; Gouveia, J. D.; Morales-García, Á.; Viñes, F.; Gomes, J. R. B.;

Illas, F. Carbon Capture and Usage by MXenes. *ACS Catal.* **2021**, *11* (17), 11248–11255. [View Article Online](https://doi.org/10.1021/ACSCATAL.1C02663) DOI: 10.1021/ACSCATAL.1C02663

(62) Sorescu, D. C.; Lee, J.; Al-Saidi, W. A.; Jordan, K. D. CO<sub>2</sub> Adsorption on TiO<sub>2</sub>(110) Rutile: Insight from Dispersion-Corrected Density Functional Theory Calculations and Scanning Tunneling Microscopy Experiments. *J. Chem. Phys.* **2011**, *134* (10), 104707. <https://doi.org/10.1063/1.3561300/70606>.

(63) Yin, W. J.; Krack, M.; Wen, B.; Ma, S. Y.; Liu, L. M. CO<sub>2</sub> Capture and Conversion on Rutile TiO<sub>2</sub>(110) in the Water Environment: Insight by First-Principles Calculations. *J. Phys. Chem. Lett.* **2015**, *6* (13), 2538–2545. <https://doi.org/10.1021/ACS.JPCLETT.5B00798>.

(64) Sorescu, D. C.; Lee, J.; Al-Saidi, W. A.; Jordan, K. D. Coadsorption Properties of CO<sub>2</sub> and H<sub>2</sub>O on TiO<sub>2</sub> Rutile (110): A Dispersion-Corrected DFT Study. *J. Chem. Phys.* **2012**, *137* (7), 74704. <https://doi.org/10.1063/1.4739088/192030>.

(65) Raupp, G. B.; Dumesic, J. A. Adsorption of Carbon Monoxide, Carbon Dioxide, Hydrogen, and Water on Titania Surfaces with Different Oxidation States. *J. Phys. Chem.* **2002**, *89* (24), 5240–5246. <https://doi.org/10.1021/J100270A024>.

(66) Wei, B.; Calatayud, M. Hydrogen Activation on Anatase TiO<sub>2</sub>: Effect of Surface Termination. *Catal. Today* **2022**, *397–399*, 113–120. <https://doi.org/10.1016/J.CATTOD.2021.11.020>.

(67) López, M.; Morales-García, Á.; Viñes, F.; Illas, F. Thermodynamics and Kinetics of Molecular Hydrogen Adsorption and Dissociation on MXenes: Relevance to Heterogeneously Catalyzed Hydrogenation Reactions. *ACS Catal.* **2021**, *11* (21), 12850–12857. <https://doi.org/10.1021/ACSCATAL.1C03150>.

(68) Fu, J.; Jiang, K.; Qiu, X.; Yu, J.; Liu, M. Product Selectivity of Photocatalytic CO<sub>2</sub> Reduction Reactions. *Mater. Today* **2020**, *32*, 222–243. <https://doi.org/10.1016/J.MATTOD.2019.06.009>.

(69) Zhang, Y.; Chen, W.; Zhou, M.; Miao, G.; Liu, Y. Efficient Photocatalytic CO<sub>2</sub> Reduction by the Construction of Ti<sub>3</sub>C<sub>2</sub>/CsPbBr<sub>3</sub>QD Composites. *ACS Appl. Energy Mater.* **2021**, *4* (9), 9154–9165. [https://doi.org/10.1021/ACSAEM.1C01406/ASSET/IMAGES/MEDIUM/AE1C01406\\_M008.GIF](https://doi.org/10.1021/ACSAEM.1C01406/ASSET/IMAGES/MEDIUM/AE1C01406_M008.GIF).

(70) Palomares, E.; Clifford, J. N.; Haque, S. A.; Lutz, T.; Durrant, J. R. Control of Charge Recombination Dynamics in Dye Sensitized Solar Cells by the Use of Conformally Deposited Metal Oxide Blocking Layers. *J. Am. Chem. Soc.* **2003**, *125* (2), 475–482.

https://doi.org/10.1021/JA027945W/ASSET/IMAGES/LARGE/JA027945WF00006J  
Article Online  
DOI: 10.1039/D5MA01122A  
PEG.

(71) Atienzar, P.; Ishwara, T.; Illy, B. N.; Ryan, M. P.; O'Regan, B. C.; Durrant, J. R.; Nelson, J. Control of Photocurrent Generation in Polymer/ZnO Nanorod Solar Cells by Using a Solution-Processed TiO<sub>2</sub> Overlayer. *J. Phys. Chem. Lett.* **2010**, *1* (4), 708–713. [https://doi.org/10.1021/JZ900356U/ASSET/IMAGES/LARGE/JZ-2009-00356U\\_0003.JPG](https://doi.org/10.1021/JZ900356U/ASSET/IMAGES/LARGE/JZ-2009-00356U_0003.JPG).

(72) Chang, X.; Wang, T.; Gong, J. CO<sub>2</sub> Photo-Reduction: Insights into CO<sub>2</sub> Activation and Reaction on Surfaces of Photocatalysts. *Energy Environ. Sci.* **2016**, *9* (7), 2177–2196. <https://doi.org/10.1039/C6EE00383D>.

(73) Hu, L.; Sai, X.; Liu, X.; Chen, Z.; Wang, G.; Yi, X. Influence of Environmental Conditions on Electrocatalytic CO<sub>2</sub> Reduction. *ChemCatChem* **2024**, *16* (6), e202301335. <https://doi.org/10.1002/CCTC.202301335>.

The data supporting the results of this study are available from the corresponding author upon reasonable request.

[View Article Online](#)  
DOI: 10.1039/D5MA01122A